Ca-Al–rich inclusions from the Ningqiang meteorite: Continuous assemblages of nebular condensates and genetic link to Type B inclusions

Y. Lin[1,*] and M. Kimura[2]

[1]Guangzhou Institute of Geochemistry, Chinese Academy of Sciences, Guangzhou 510640, China
[2]Institute of Astrophysics and Planetary Science, Faculty of Science, Ibaraki University, Mito 310, Japan

Abstract—The petrography and mineral chemistry of 110 Ca-, Al-rich inclusions (CAIs) and 9 Ca- and/or Al-rich amoeboid olivine aggregates (AOAs) from the Ningqiang carbonaceous chondrite are reported. These CAIs are referred to as hibonite-bearing and hibonite-free melilite–spinel–rich (Type A), and spinel–pyroxene inclusions. Melilite is more gehlenitic in the hibonite-bearing Type As than in the other two types, and all of them vary within a range of $Åk_{0-30}$. Modal compositions of the three types of CAIs overlap with each other, and make up a continuum with wide ranges of melilite: spinel: diopside. The diopside occurs as rims on the CAIs or their individual concentric objects. The 9 AOAs contain spinel $\pm$ diopside $\pm$ anorthite in the centers of the aggregates; the spinel grains rimmed by diopside in the centers are similar to the spinel–pyroxene inclusions. Bulk compositions of these CAIs vary along the condensation trajectory, with the hibonite-bearing Type As plotting at the beginning followed by hibonite-free Type As then by spinel–pyroxene inclusions as temperature decreases. Bulk compositions of the AOAs are close to the lowest temperature condensation trajectory. Except for a few with compact textures, most of the Type As and spinel–pyroxene inclusions are fluffy aggregates, probably pristine vapor-solid condensates of the nebula.

The bulk compositions of the Type As appear to overlap with the range of most melilite–Ti–Al–clinopyroxene–rich (Type B) inclusions. Hence, crystallization of liquids produced by melting the Type As can form Type B inclusions, without significant evaporative loss of MgO or SiO_2. A few Type Bs have bulk compositions deviating from the range of their proposed precursors, and may have suffered significant evaporation, as suggested in previous studies. *Copyright © 2003 Elsevier Science Ltd*

1. INTRODUCTION

Ca-, Al-rich inclusions (CAIs) are the most extensively studied components of carbonaceous chondrites. They can be divided into coarse-grained and fine-grained inclusions (Grossman, 1975; Grossman and Ganapathy, 1975). The most common coarse-grained inclusions in CV chondrites are Type A (melilite-predominant), Type B (melilite–Ti–Al–clinopyroxene–rich) (Grossman, 1975) and Type C (Ti–Al–clinopyroxene–anorthite–rich) (Wark, 1987). Furthermore, most Type A inclusions are highly irregular and convoluted in shape, and consist of multiple independently rimmed objects; they are referred to as fluffy Type A (FTA) (MacPherson and Grossman, 1984). Correspondingly, other spheroidal or irregular Type As with compact textures are referred to as compact Type A (CTA). The most abundant fine-grained inclusions in CV chondrites are spinel–pyroxene inclusions (Grossman and Ganapathy, 1975, 1976) and amoeboid olivine aggregates (AOAs) (Grossman and Steele, 1976). FTAs and AOAs are the most likely to be aggregates of nebular condensates (Grossman and Steele, 1976; MacPherson and Grossman, 1984), whereas Type C inclusions probably crystallized from melts (Wark, 1987), which were produced by melting altered Type As (Beckett and Grossman, 1988), i.e., the anorthite–spinel–rich inclusions (ASIs) (Lin and Kimura, 1998). However, the origins of other types of CAIs and genetic relationships among them are long-standing problems. In addition, few bulk chemical composi-

tions and modal compositions of FTAs and fine-grained inclusions have been reported. Limited data of Type As (mostly CTAs) show a narrow range in the spinel-projected gehlenite–anorthite–forsterite ternary plane (Stolper, 1982), and this can be expected based on their modal compositions that are melilite-predominant with spinel and perovskite. These bulk compositions plot at the beginning of the condensation trajectory (Grossman et al., 2000).

All Type B inclusions probably crystallized from liquids (Grossman, 1975; MacPherson and Grossman, 1981; Wark and Lovering, 1982), and some of them show evidence for multiple heating events (Podosek et al., 1991; MacPherson and Davis, 1993; Beckett et al., 2000; Lin and Kimura, 2000). However, the precursors of Type Bs are controversial. One possibility is that Type Bs are refractory residues of MgO-, SiO_2-rich materials that were partially or completely melted and suffered significant evaporation (Wark and Lovering, 1982). Bulk compositions of most Type Bs can be produced by non-equilibrium evaporative loss of SiO_2 and MgO of liquid droplets with compositions on a possible equilibrium condensation trajectory (Grossman et al., 2000). Although mass fractionation of isotopes of Mg and Si supports the high-temperature evaporation origin of Type Bs (Grossman et al., 2000), the isotopic data are rarely combined with known bulk chemical compositions of the same CAIs. Furthermore, the proposed MgO-, SiO_2-rich materials are not identified or related to assemblages in carbonaceous chondrites. Alternatively, Type Bs might crystallize from CaO-MgO-Al_2O_3-SiO_2 (CMAS) liquids that condensed from the nebula (Yoneda and Grossman, 1995). The condensation of

* Author to whom correspondence should be addressed (linyt@gig.ac.cn).

CMAS liquid requires some extreme conditions of either elevated pressures or enhanced dust/gas ratios.

CTAs probably either experienced solid-state crystallization or were once molten (MacPherson and Grossman, 1984; Simon et al., 1999). Although most CTAs are dominated by melilite or >60 vol% after Simon et al., 1999) and are clearly distinguished from the Ti–Al–clinopyroxene–rich Type Bs, there is a continuum in bulk chemical compositions between Type A and B inclusions (Mason and Taylor, 1982; Grossman et al., 2000). This suggests that there may be a genetic relationship between the once molten CTAs and Type Bs. Origins of spinel–pyroxene inclusions are also controversial. Some authors suggest that they are aggregates of vapor-solid condensates (MacPherson et al., 1983; MacPherson and Davis, 1994; Weber and Bischoff, 1997), while others argue that spinel–pyroxene inclusions crystallized from liquids produced by melting refractory condensates (Greenwood et al., 1994), or by melting and evaporating MgO-, SiO_2-rich materials (Kornacki and Fegley, 1984; Kornacki and Wood, 1985). To test hypotheses for the origin of spinel–pyroxene inclusions and their genetic relationship with other CAIs, it is important to determine their bulk chemical compositions and petrologic and mineralogical characteristics.

The Ningqiang meteorite has been classified as a CV-anomalous (e.g., Rubin et al., 1988; Weisberg et al., 1996) or a CK-anomalous (Kallemeyn et al., 1991). It closely resembles the Allende CV3 chondrite and contains products of secondary alteration similar to those in Allende and other CV3 chondrites (Weisberg et al., 1996; Kimura et al., 1997). Ningqiang contains a significantly higher abundance ratio of AOAs to chondrules than other CV3s (Rubin et al., 1988), which may suggest it preserves relatively more pristine assemblages of nebular condensates, although no direct evidence for genetic relationship between non-molten AOAs and once-molten chondrules. This is supported by discovery of the proposed precursors of Type C inclusions, i.e., the anorthite–spinel–rich inclusions (ASIs) in Ningqiang (Lin and Kimura, 1998). During our systematic study of the Ningqiang meteorite, a large number of CAIs were found. These CAIs include petrographic types similar to those from Allende, but which are less altered and less abundant (2.5 vol%) (Lin and Kimura, 1997a, 1998, 2000). Here, we focus on the other CAIs, to determine if they are pristine assemblages of gas-solid condensates and to evaluate their genetic relationship with Type Bs. Preliminary results of this study were reported by Lin and Kimura (1997b).

2. SAMPLES AND EXPERIMENTS

A total of 124 Ca-, Al-rich inclusions (CAIs) were identified from 21 thin sections displaying a total surface area of 17.4 cm^2 of the Ningqiang carbonaceous chondrite. We determined a CAI abundance of 2.5 vol%, higher than a previous estimate of $1.0^{+1.0}_{-0.5}$% (Rubin et al., 1988). The CAIs studied include 2 Type Bs (Lin and Kimura, 2000), 2 POIs (Lin and Kimura, 1997a), 9 ASIs and their fragments (Lin and Kimura, 1998), 1 Type C inclusion (Lin and Kimura, 1998), and another 110 inclusions that are the subject of this study. Besides the 110 CAIs, 9 spinel/anorthite/diopside-bearing amoeboid olivine aggregates (hereafter refractory AOAs) were also studied for comparison.

All CAIs and refractory AOAs were observed using the JEOL 733 electron probe microanalyzer (EPMA), equipped with a backscattered electron detector and three wavelength dispersive spectrometers, in SEM mode. Modal compositions of more than half of the CAIs were calculated from areas of the constituent phases on the backscattered

electron images. The remaining CAIs have very small grain sizes and/or are significantly altered, hence it is difficult to quantitatively determine their modal compositions. Quantitative analyses of minerals were conducted using the EPMA at 20 nA and 15kV. Peak overlapping of the K_α line of V by the K_β line of Ti was corrected, and the data were processed by the Bence-Albee method. The detection limits (1σ) are 0.01 wt% for K_2O; 0.02 wt% for SiO_2, Al_2O_3, V_2O_3, MgO, CaO, Na_2O and Cl; 0.03 wt% for TiO_2 and Cr_2O_3; 0.05 wt% for FeO; 0.06 wt% for NiO and MnO; 0.10 for ZnO.

Simon et al. (2002) reported bulk compositions of a few large Types A and B CAIs based on INAA data of the excavated samples, reconstructed modal compositions and mean EPMA data of individual phases of the multi-sections. However, the majority of the CAIs and refractory AOAs from the Ningqiang meteorite are small in size, irregular in shape and heterogeneous in mineral chemistry, hence broad beam analysis was used to determine bulk compositions in this work. The defocused beam has a diameter of 20 or 50 μm according to sizes of the CAIs and AOAs. The analysis positions of each assemblage was carefully selected to cover the whole area and avoid beam overlapping onto the adjacent meteorite matrix. The integrated counts of each element of the individual CAIs and refractory AOAs were also corrected by the Bence-Albee method. Effects of heterogeneous matrix (Albee et al., 1977) and the different densities of the constituent phases (Ikeda, 1980) were not corrected in this work, because of the lack of modal compositions for many of the CAIs and AOAs and their highly heterogeneous mineral compositions. We estimate that this results in an error of less than 10% for the major elements SiO_2, CaO, Al_2O_3 and MgO, according to the combined correction factors estimated for Na_2O 0.76–0.80, SiO_2 0.86–0.97, CaO 0.94–1.0, Al_2O_3 1.0–1.1, MgO 1.1, TiO_2, Cr_2O_3 and FeO 1.1–1.2 (Lin and Kimura, 1998). Heterogeneity of the CAIs may cause less spinel to be sampled for spinel–pyroxene inclusions because this mineral usually occurs in the centers of the inclusions, or more spinel for Type As if they have a spinel layer adjacent to the rims of the CAIs. However, this under- or oversampling of spinel does not change where the bulk compositions of the CAIs plot on the spinel-projecting gehlenite–anorthite–forsterite triangle diagram. It is also possible that diopside rims of CAIs are oversampled due to sections shifting from the cores of CAIs, or undersampled because parts of the diopside rims may not be integrated to avoid the beam overlapping the adjacent matrix material.

3. RESULTS

3.1. Petrography

All of the CAIs studied here consist of melilite, spinel and Ca-rich pyroxene in varying abundances. Ca-rich pyroxene occurs as rims on single CAIs or on individual concentric objects of complex CAI aggregates, similar to the diopside layer typical of Wark-Lovering rims (Wark and Lovering, 1977) and different from the subliquidus Ti–Al–clinopyroxene inside Type B and C inclusions. Perovskite is the most common accessory phase, and hibonite and grossite were found only in a few CAIs. The degree of alteration of melilite to produce feldspathoids ± diopside ± hedenbergite is highly variable among inclusions. The inclusions range from containing nearly unaltered melilite to having little melilite remaining. Another common alteration reaction is the substitution of MgO by FeO in spinel. Wollastonite and anorthite are less common alteration products replacing melilite. No phyllosilicate or ilmenite was found in Ningqiang.

Figure 1 shows the modal compositions of the CAIs. Their composition varies between almost endmember melilite, diopside and spinel, and shows no clear cutoff or groups. Most CAIs or their constituent objects have similar concentric structures and mineral sequences from core to rim (see below), regardless of the heterogeneous modal compositions. We arbitrarily classify the CAIs with melilite <10 vol% and/or diop-
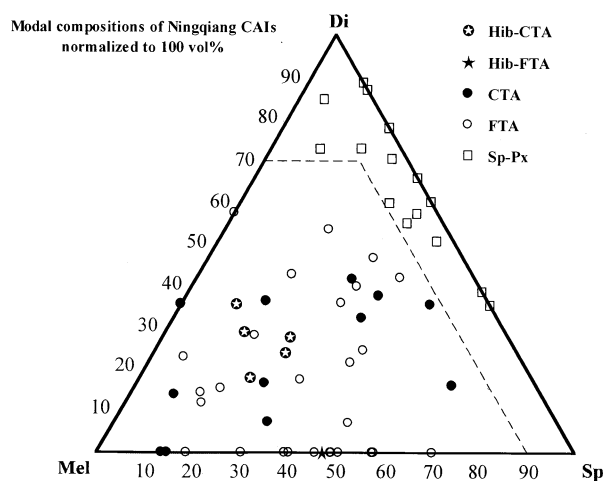
Fig. 1. Modal compositions of Type A and spinel–pyroxene inclusions in Ningqiang. Type A inclusions are divided into hibonite-bearing and hibonite-free subtypes base on the presence of hibonite (Hib), and are referred to as fluffy subtype (FTA) and compact subtype (CTA) based on their textures. The other abbreviations are: melilite (Mel), diopside (Di), spinel (Sp) and pyroxene (Px). The dashed line shows the arbitrary range of spinel–pyroxene inclusions. Note the continuous variation of the modal compositions within and between the types.

side >70 vol% as spinel–pyroxene inclusions, and the others as Type As. Assignation of other CAIs without quantitative modal compositions is estimated by visual comparison with the above classified CAIs. The spinel–pyroxene inclusions are identical to their counterparts in other carbonaceous chondrites. However, many of the Type As from Ningqiang contain much less melilite than typical melilite-predominant Type As. The low abundance of melilite in Ningqiang Type As is partially due to the presence of diopside rims. On the other hand, a wide range of the modal compositions for fluffy Type As from Allende has been noted (MacPherson and Grossman, 1984). Some of these contain more spinel than melilite, in contrast to typical melilite-predominant Type As.

Based on the presence of hibonite, we divide the Type A CAIs into two subtypes, i.e., hibonite-bearing and hibonite-free. Furthermore, they are depicted as compact or fluffy based on their compact or loose textures following the scheme of CTA and FTA inclusions from Allende (MacPherson and Grossman, 1984). The bulk compositions of 73 CAIs and 9 refractory AOAs are listed in Table 1. The other CAIs were not analyzed due to their high degree of alteration and/or loose structures that cause the defocused electron beam to overlap onto the adjacent clastic matrix.

3.1.1. Hibonite-Bearing Type A

Eight of the Type A inclusions that were studied contain minor hibonite. All of them are melilite-rich (~>50 vol%), with less abundant spinel (<50 vol%) and diopside (<35 vol%). Minor perovskite occurs in all hibonite-bearing Type As, but grossite is only present in two of them. Bulk compositions of the hibonite-bearing Type As are CaO-, Al$_2$O$_3$-rich and SiO$_2$-, MgO-poor (Table 1).

Two hibonite-bearing Type As are irregularly shaped,

loosely packed assemblages of concentrically layered objects, hence referred to as fluffy type A inclusions. The larger one, NQJ3-3-4, is 850 × 1730 μm in size (Fig. 2a), and consists of numerous concentric objects with sizes that range from 20 to 350 μm. All of the objects have diopside rims (~4–6 μm wide), and their mineralogy varies from melilite-rich to spinel-rich. Figure 2b is close-up of the largest object, consisting of a melilite core surrounded by layers of spinel, melilite and diopside in sequence. Most laths of hibonite, anhedral grains of grossite and small grains of perovskite are enclosed in the melilite in the core, but some (except grossite) are also embedded in the spinel layer (<30 μm wide). Another fluffy hibonite-bearing Type A inclusion (NQL1-4-1, 730 × 1100 μm) is also composed of several concentric objects. Some objects have a melilite core surrounded by a layer of spinel, and others have small grains of melilite embedded in spinel. Laths of hibonite and small grains of perovskite are enclosed in the spinel layer or associate with melilite in the core. NQL1-4-1 has no Ca-rich pyroxene rim. In spite of their loosely packed structures, neither of these CAIs is heavily altered. Another hibonite-bearing Type A inclusion (NQL2-3-11, 50 × 110 μm) is a single object consisting of melilite, spinel and diopside, with a few laths of hibonite enclosed in melilite. The melilite is significantly altered to feldspathoids, especially along the surface of the inclusion. This CAI is similar to the single concentric object of NQJ3-3-4 (except for the absence of grossite), hence it is referred to as fluffy type too.

The other five hibonite-bearing Type As show compact textures (Fig. 2c). However, all of them are irregular in shape, different from the rounded shapes of typical compact Type As from Allende. All five CAIs are concentrically layered, consisting of a melilite core surrounded by a layer of spinel (<20 μm) then rimmed by diopside (5–10 μm). Minor melilite is often found between the spinel layer and diopside rim. Of the five hibonite-bearing CAIs, NQJ3-5-7 is unique, containing a grain of Sc$_2$O$_3$-rich Ti–Al–clinopyroxene (16.4 wt% Sc$_2$O$_3$) in melilite and accessory highly Ti, Al-rich clinopyroxene rims around perovskite (Lin et al., 2003). Minor hibonite occurs as laths in the spinel layer. The other four CAIs, i.e., NQJ3-3-1.2, NQJ3-3-1.3, NQJ3-3-1.4 and NQJ3-3-1.5, have a close spatial relationship and similar bubble-like voids in melilite in the cores (Fig. 2c). Hibonite is enclosed in the melilite, whereas it occurs in spinel in NQJ3-5-7. A small grain of grossite was found in melilite in NQJ3-3-1.3. Perovskite occurs as small grains mainly in the melilite close to the spinel layer, except for several large lumps (20–40 μm) in NQJ3-3-1.4, a fragmental CAI. It is possible that these four hibonite-bearing Type As are genetically related.

3.1.2. Hibonite-Free Type A

More than half of the CAIs (71 out of 124) in Ningqiang are classified as hibonite-free Type A. Most of them (53 out of 71) are irregularly shaped and concentrically layered objects or loosely packed assemblages of concentrically layered objects, hence referred to as fluffy type A inclusions. The mineral sequences of these objects are, from core to rim, ±melilite, spinel, ±melilite, and ±diopside. Minor perovskite is enclosed in melilite and/or spinel usually in the centers. In addition, several CAIs have a layer of olivine outside the diopside rim,

Table 1. Bulk compositions of CAIs and refractory AOAs from Ningqiang (wt%).[a]

Types	Object	dL[b] (μm)	SiO$_2$	TiO$_2$	Al$_2$O$_3$	Cr$_2$O$_3$	FeO	MnO	MgO	CaO	Na$_2$O	K$_2$O	Cl
Hibonite-bearing CTA													
	NQJ3-3-1.2	622	25.0	1.52	34.7	b.d.	0.93	b.d.	4.25	32.9	0.60	b.d.	0.09
	NQJ3-3-1.3	334	17.3	1.79	43.3	b.d.	0.69	b.d.	8.75	28.0	0.16	b.d.	b.d.
	NQJ3-3-1.5	502	21.9	1.67	37.4	b.d.	0.58	b.d.	5.59	32.5	0.33	b.d.	b.d.
	NQJ3-5-7	833	25.3	3.60	33.0	b.d.	2.58	b.d.	9.48	25.4	0.61	b.d.	0.09
Hibonite-bearing FTA													
	NQL1-4-1	989	16.7	2.00	41.9	1.31	1.22	b.d.	10.4	25.8	0.58	0.03	0.03
	NQL2-1-1	950	24.4	0.53	35.1	2.48	8.24	b.d.	10.7	17.2	1.03	0.12	0.17
	NQJ3-3-4[c]	1369[e]	13.5	2.43	51.0	b.d.	1.64	b.d.	4.81	26.5	0.16	b.d.	0.03
	NQJ3-3-4[d]	1369	18.3	1.96	41.9	b.d.	0.20	b.d.	4.65	33.0	b.d.	b.d.	b.d.
Hibonite-free CTA													
	NQJ2-1-4	265	17.0	2.01	45.7	b.d.	1.04	b.d.	15.6	18.5	0.15	b.d.	b.d.
	NQJ3-12-11	158	15.5	1.22	50.6	0.19	1.80	b.d.	20.5	9.71	0.47	b.d.	b.d.
	NQJ3-12-20	246	26.2	1.39	31.4	0.15	1.33	b.d.	7.31	31.4	0.69	b.d.	0.06
	NQJ3-5-16	105	28.4	1.30	30.1	0.95	10.8	0.07	13.9	11.3	2.60	0.08	0.44
	NQJ3-5-9	606	17.8	2.13	42.7	b.d.	0.56	b.d.	10.0	26.7	0.10	b.d.	b.d.
	NQL1-8-14.2	71	17.4	6.82	40.6	1.18	2.20	b.d.	15.1	16.2	0.51	0.02	b.d.
	NQL2-6-8	294	22.6	0.67	34.4	1.33	0.39	b.d.	1.82	38.3	0.49	b.d.	0.08
	NQL2-7-4	265	15.1	4.92	42.6	1.77	1.03	b.d.	11.7	22.6	0.38	b.d.	b.d.
	NQW1-20	170	31.4	2.19	24.6	1.20	2.22	b.d.	10.2	27.4	0.54	b.d.	0.16
	NQW2-5	247	31.1	2.03	27.3	0.70	2.06	b.d.	11.2	25.1	0.40	0.02	0.06
	NQW3-9	1450	19.4	1.07	39.2	0.94	0.59	b.d.	7.06	31.5	0.21	0.02	0.05
	NQW4-5	60	20.9	1.10	42.8	0.59	1.23	b.d.	18.3	14.7	0.33	0.02	b.d.
Hibonite-free FTA													
	NQJ2-1-10	320	33.9	3.71	19.1	0.14	9.53	b.d.	10.0	21.7	1.79	0.14	0.07
	NQJ2-1-5	531	35.1	0.94	21.4	0.23	7.82	b.d.	9.11	23.5	1.66	0.04	0.22
	NQJ3-12-4	267	32.6	1.00	25.2	b.d.	5.56	b.d.	7.79	25.9	1.80	0.10	0.07
	NQJ3-12-5	499	30.1	1.33	26.9	b.d.	3.43	b.d.	6.84	30.3	0.99	0.06	0.07
	NQJ3-12-6	474	22.4	1.14	37.6	b.d.	4.63	b.d.	8.59	24.5	1.03	0.07	b.d.
	NQJ3-12-8	267	23.9	1.39	38.0	0.11	2.52	b.d.	15.1	18.1	0.79	b.d.	0.11
	NQJ3-5-12	332	32.5	0.92	24.8	0.26	5.62	b.d.	9.55	25.7	0.57	b.d.	0.03
	NQJ3-5-14	147	38.8	1.05	19.8	b.d.	4.13	b.d.	13.1	21.5	1.39	b.d.	0.25
	NQJ3-5-5	633	45.3	1.03	11.2	b.d.	5.58	b.d.	13.2	21.0	2.22	b.d.	0.39
	NQJ3-5-6	335	16.2	1.96	48.2	0.09	2.11	b.d.	17.3	14.0	0.14	b.d.	b.d.
	NQJ3-5-8	794	26.7	1.19	31.1	b.d.	1.14	b.d.	7.59	32.1	0.15	b.d.	b.d.
	NQL1-6-11	653	25.8	0.93	31.8	0.84	7.36	b.d.	9.63	22.3	1.16	0.06	0.15
	NQL1-6-18	219	36.8	1.64	21.4	0.99	4.02	b.d.	11.4	23.2	0.42	b.d.	0.10
	NQL1-8-11	556	26.2	1.27	33.2	1.07	5.98	b.d.	13.7	17.4	1.06	0.05	0.09
	NQL1-8-7	323	26.7	2.04	31.9	0.92	6.23	b.d.	14.9	16.5	0.73	0.05	0.10
	NQL2-1-6	103	42.9	1.30	11.9	1.67	5.76	b.d.	13.3	21.3	1.53	0.09	0.26
	NQL2-3-10	864	11.0	3.26	52.4	1.76	6.38	b.d.	18.6	6.36	0.26	b.d.	b.d.
	NQL2-3-3	523	33.6	1.15	25.7	1.60	1.78	b.d.	18.0	18.1	b.d.	b.d.	b.d.
	NQL2-7-1	152	21.9	1.50	35.5	1.52	2.45	b.d.	12.5	24.2	0.45	b.d.	b.d.
	NQL2-7-5	195	30.9	1.38	27.0	1.10	1.46	b.d.	11.6	26.2	0.42	b.d.	b.d.
	NQL2-7-7	1543	37.1	1.36	19.5	1.36	6.63	b.d.	10.9	21.1	1.78	b.d.	0.30
	NQW1-1	315	28.6	1.51	29.9	0.45	2.13	b.d.	9.19	27.3	0.82	b.d.	0.10
	NQW1-14	159	25.0	2.10	33.1	0.29	2.90	b.d.	8.27	27.5	0.68	0.02	0.13
	NQW1-16	175	31.1	1.16	27.4	0.88	3.75	0.04	13.0	21.7	0.79	0.03	0.10
	NQW1-19	373	14.1	4.23	44.2	0.59	5.42	b.d.	12.0	18.8	0.49	0.03	0.12
	NQW1-2	228	26.9	1.19	31.4	1.03	6.28	b.d.	13.4	18.9	0.86	0.05	0.09
	NQW1-22	320	42.8	0.16	12.2	0.46	8.56	0.36	14.7	18.7	1.63	0.16	0.28
	NQW1-24	203	28.7	2.32	27.5	0.66	2.97	0.08	6.45	30.7	0.56	0.05	0.06
	NQW1-3	501	9.12	1.91	55.4	0.56	4.26	b.d.	17.7	10.3	0.68	b.d.	0.07
	NQW1-7	1333	24.2	0.65	36.1	0.65	3.66	0.08	15.3	18.8	0.52	0.02	0.11
	NQW2-2	96	14.1	2.59	49.6	0.80	3.13	b.d.	17.2	12.5	0.07	b.d.	0.06
	NQW3-10	108	21.9	2.14	36.9	0.81	6.13	b.d.	14.5	16.9	0.62	0.07	0.02
	NQW3-13	119	23.3	1.81	37.3	1.16	7.41	b.d.	16.2	11.6	1.04	0.02	0.13
	NQW3-2	375	34.5	0.97	21.4	0.35	3.93	b.d.	7.01	29.2	2.13	0.05	0.35
	NQW3-8	650	34.5	1.42	23.0	0.45	3.59	b.d.	9.10	26.1	1.47	0.02	0.27
	NQW4-1	786	24.8	1.96	34.4	0.75	1.50	b.d.	10.3	25.6	0.60	0.05	0.06
Spinel-pyroxene-rich													
	NQJ3-12-1	1855	40.8	0.49	14.7	0.28	6.19	b.d.	21.1	15.8	0.56	0.04	0.04
	NQJ3-12-16	339	32.1	1.12	29.7	0.19	2.21	b.d.	18.7	15.7	0.33	b.d.	b.d.
	NQJ3-5-10	245	40.3	0.98	18.3	0.07	4.13	b.d.	16.7	19.1	0.35	b.d.	0.03
	NQJ3-5-11	430	28.4	0.97	33.2	0.32	4.69	b.d.	17.6	14.4	0.39	b.d.	0.05
	NQJ3-5-18	207	21.0	1.88	37.1	0.15	14.5	b.d.	16.2	8.58	0.57	0.02	b.d.
	NQL1-6-2	564	20.4	1.20	43.8	1.11	4.51	b.d.	18.7	10.2	0.04	b.d.	0.05

Table 1. (Continued)[a]

Types	Object	dL[b] (μm)	SiO$_2$	TiO$_2$	Al$_2$O$_3$	Cr$_2$O$_3$	FeO	MnO	MgO	CaO	Na$_2$O	K$_2$O	Cl
	NQL1-6-6	351	33.3	0.67	20.7	1.15	8.11	0.09	28.0	7.54	0.41	b.d.	0.12
	NQL2-1-3	121	21.5	2.96	39.6	1.56	3.53	b.d.	18.3	12.4	0.06	b.d.	b.d.
	NQL2-1-9	188	38.3	1.34	19.8	0.87	2.16	b.d.	17.2	19.9	0.32	b.d.	b.d.
	NQL2-3-6	42	36.0	1.02	19.6	1.19	10.7	0.08	13.2	14.3	3.30	0.04	0.65
	NQL2-3-9	74	13.9	1.77	49.3	1.54	8.15	b.d.	18.0	6.84	0.39	0.04	b.d.
	NQL2-4-3	283	48.8	0.95	6.32	1.03	4.54	b.d.	14.8	22.5	0.81	0.07	0.12
	NQW1-10	498	29.8	0.25	29.0	0.51	10.1	0.09	15.7	13.3	1.07	0.06	0.24
	NQW1-23	50	29.8	0.76	30.5	1.80	5.78	b.d.	15.2	15.8	0.36	b.d.	0.05
	NQW1-4	391	28.8	0.96	25.7	0.65	19.0	0.22	17.1	5.19	2.20	0.07	0.20
	NQW1-5	1051	39.0	1.06	20.6	0.66	1.97	b.d.	16.8	19.5	0.41	0.02	b.d.
	NQW2-1	443	37.4	1.42	20.7	0.55	6.14	0.16	12.0	19.2	2.00	0.08	0.46
	NQW3-6	87	10.7	0.53	53.8	0.23	9.82	b.d.	19.1	4.88	0.79	0.05	0.05
	NQW4-2	383	42.2	1.33	10.8	0.29	12.5	0.12	13.6	16.9	1.76	0.08	0.42
AOA														
	NQJ2-1-12	1030	39.7	0.23	10.1	0.13	5.16	b.d.	36.7	7.10	0.65	b.d.	0.14
	NQJ3-5-15	964	38.6	0.16	3.94	0.23	17.5	b.d.	36.4	3.09	0.10	b.d.	b.d.
	NQJ3-5-17	319	32.2	b.d.	2.34	0.66	45.3	0.29	17.1	1.98	0.11	b.d.	b.d.
	NQW3-14	269	41.8	0.48	11.7	1.23	5.16	b.d.	25.5	13.3	0.72	0.02	0.11
	NQW3-4	251	40.5	0.55	7.56	1.28	7.01	0.06	33.2	9.20	0.50	b.d.	0.12
	NQJ3-3-2	2296	23.7	1.67	40.4	0.29	1.23	b.d.	20.6	12.1	b.d.	b.d.	b.d.
	NQL1-6-15	857	39.6	0.42	10.5	1.08	3.66	b.d.	36.0	8.75	b.d.	b.d.	b.d.
	NQL1-6-3	1173	39.2	0.44	10.2	0.91	3.24	b.d.	38.3	7.81	b.d.	b.d.	b.d.
	NQW3-1	1093	39.7	0.49	11.3	0.73	3.85	b.d.	33.5	10.1	0.27	b.d.	0.03

[a] Normalized to 100%, b.d. = below the detection limits.
[b] Diameters of circles that have similar areas of the irregular CAIs.
[c] The largest concentric object.
[d] The second largest concentric object.
[e] Size of the whole inclusion.

or enclosed in the latter. The widths of the diopside rims are rather constant (~4–10 μm), regardless of sizes and modal compositions of the CAIs. The abundances of melilite, spinel and diopside vary continuously from melilite-rich (Figs. 3a,b) to spinel-rich (Fig. 3c,d) to diopside-rich (Fig. 3e). Furthermore, this wide range of compositions is also found among individual objects in the same CAIs (Figs. 2a, 3e,f). In fact, the melilite-rich fluffy Type As are identical to their hibonite-bearing counterparts, except for the lack of hibonite and grossite in the former. The degree of alteration is highly variable among the inclusions, some have mostly melilite replaced by fine-grained feldspathoids and diopside, whereas others are essentially unaltered. The degree of the alteration is not related to the presence of diopside rims that might protect the melilite from reaction with the nebular gas and/or mobile components of the matrix. Some fragmental CAIs have unaltered melilite in contact with the clastic matrix (Fig. 3b), suggesting that alteration did not take place in the parent body. These fluffy Type As are similar to their counterparts from Allende (MacPherson and Grossman, 1984), although the Ningqiang inclusions extend to more spinel- and/or diopside-rich compositions.

The other 18 Type A inclusions (Fig. 3g) show compact textures and are referred to as compact type A inclusions. They are irregular in shape except for four small melilite–spinel–rich spheres (60–170 μm in diameter). Both the largest CTA (NQW3-9, 1.1 × 1.5 mm) and the largest melilite–spinel–rich sphere (NQW1-20, 170 μm in diameter) are unique, with highly Ti, Al-rich clinopyroxene rims around perovskites enclosed in melilite in the former and V-rich Ti–Al–clinopyroxenes in melilite in the latter (Lin et al., 2003). Many other

CTAs are similar to the single concentric objects of FTAs, except for their compact textures. In fact, the CTAs overlap with the FTAs in their modal and bulk chemical compositions (Figs. 1 and 9). Moreover, it is noted that objects like the other three small melilite–spinel-spheres can also be found in several fluffy Type As. The mineral sequence of these concentric CTAs is, from core to rim, ±melilite, spinel, ±melilite, and ±diopside. Most CTAs shows little alteration of melilite, mainly resulting in formation of feldspathoids and diopside.

3.1.3. Spinel-Pyroxene Inclusions

Spinel–pyroxene inclusions are the second most abundant type of inclusion, with 31 examples found in this study. All of the spinel–pyroxene inclusions are concentrically layered objects or loose assemblages of objects. Each object consists of a spinel core rimmed by diopside (5–20 μm in width). Eleven inclusions have an additional olivine layer outside the diopside rim. Minor melilite is found in 15 of the spinel–pyroxene inclusions. In 7 inclusions of them, melilite is enclosed in spinel and/or intergrows with the latter in the cores; in the other CAIs, minor melilite occurs between the spinel core and the diopside rim. Perovskite is rare, small and enclosed in spinel. Hibonite laths were found in only one spinel–pyroxene inclusion (NQL1-6-6), and they are intergrown with the spinel in the core. Anorthite is found between spinel and the diopside rims, probably as an alteration product replacing melilite. It is noted that the spinel–pyroxene inclusions form a continuum with fluffy Type As, with regard to the concentric structures, modal mineralogy, bulk composition, and mineral chemistry (see next
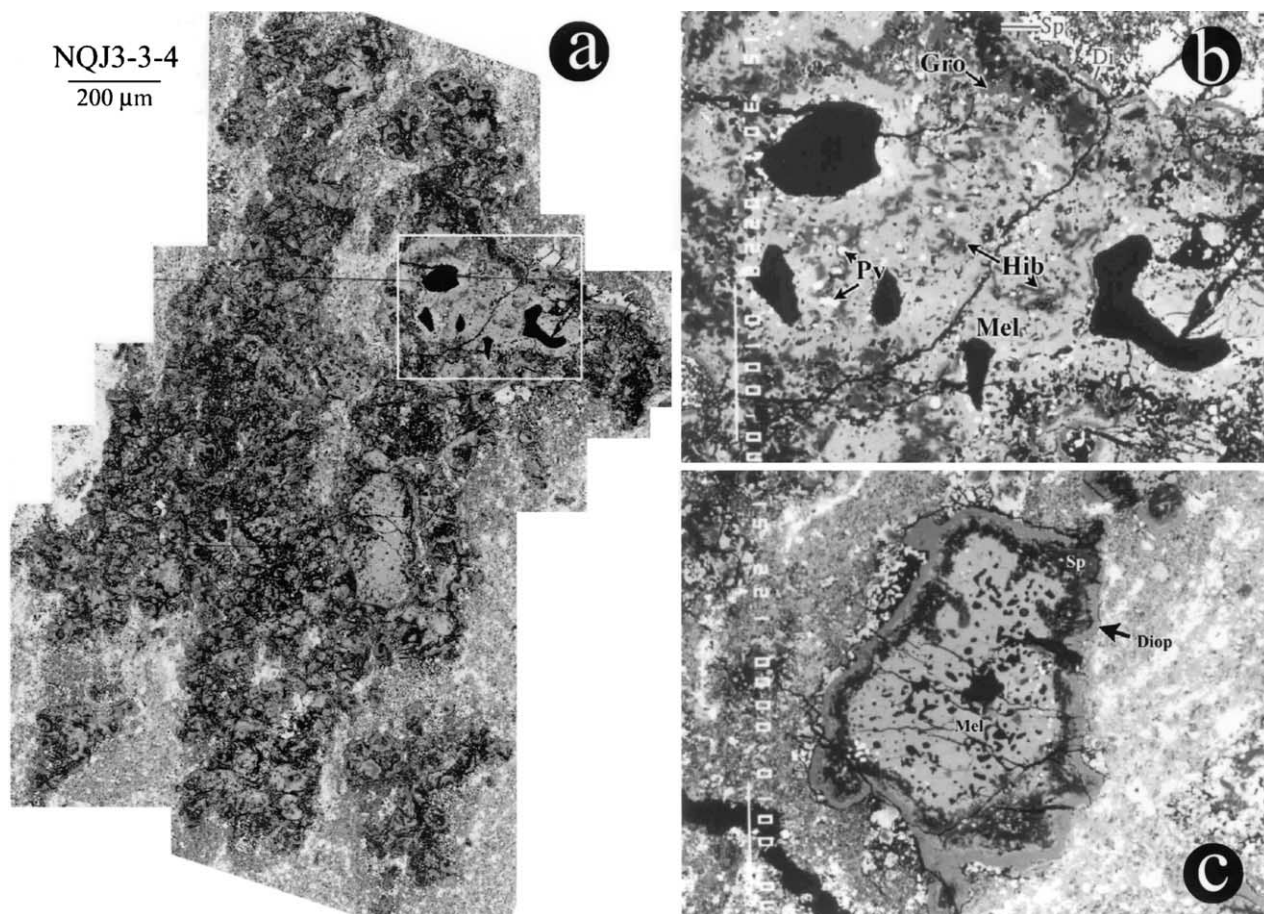
Fig. 2. Backscattered electron (BSE) images of hibonite-bearing Type A inclusions. (1) A fluffy hibonite-bearing Type A (NQJ3-3-4), consisting of numerous concentrically layered objects with various sizes. Width of the view is 1.44 mm. (b) Inset of the largest concentric object in NQJ3-3-4. Laths of hibonite (Hib), anhedral grossite (Gro) and small grains of perovskite (Pv) are enclosed in melilite (Mel) mainly in the center of the inclusion. Outward, there are a spinel (Sp) layer and a diopside (Di) rim. Dark black areas are voids. Width of the view is 380 μm. (c) A compact hibonite-bearing Type A (NQJ3-3-1.3), consisting of a melilite core, a spinel layer and a diopside rim. Minor hibonite is enclosed in the melilite (not see here). White grains in melilite along the boundary adjacent to the spinel layer are perovskite. Note the black and bubble-like voids in melilite. Width of the view is 400 μm.

subsection). The melilite-bearing spinel–pyroxene inclusions (Figs. 4a,b) are compositionally continuous with the melilite-poor fluffy Type As. Some spinel–pyroxene inclusions also extend to diopside-rich compositions (Figs. 1, 4c,d)

3.1.4. Refractory AOAs

Amoeboid olivine aggregates (AOAs) were reported to be common in thin sections of Ningqiang (Rubin et al., 1988). In this study, we focused only on those AOAs that contain spinel $\pm$ diopside $\pm$ anorthite, and refer to these as refractory AOAs. Nine refractory AOAs were found in this study. Spinel $\pm$ diopside $\pm$ anorthite tend to concentrate in the centers of the AOAs. In the spinel-bearing AOAs, mineral coexistence varies from spinel–pyroxene in the center to pyroxene-anorthite close to the rim (Figs. 5a,b). The spinel-bearing core is a loose assemblage of spinel grains with diopside rims (Fig. 5b), similar to the spinel–pyroxene inclusions depicted above. Diopside usually intergrows with anorthite, and both are enclosed in olivine (Fig. 5c). The spinel–pyroxene inclusions, spinel-bear-

ing AOAs, and diopside-anorthite-bearing AOAs seem to form a continuous trend in texture and modal composition.

3.2. Mineral Chemistry

3.2.1. Hibonite

Besides CaO (8.01–8.85 wt%) and Al_2O_3 (78.1–89.3 wt%), hibonite contains MgO (1.17–3.52 wt%) and TiO_2 (1.45–7.21 wt%). The MgO and TiO_2 contents are positively correlated with each other (Fig. 6), and both are lower than those in the spinel-hibonite-nodule in Type B CAI NQJ3-5-4 in Ningqiang (Lin and Kimura, 2000). The composition of hibonite in FTA NQJ3-3-4 appears to differ with textural setting. The laths coexisting with grossite in the cores of the concentric objects contain less MgO (3.05–5.17 wt%) and TiO_2 (2.06–3.28 wt%) than those embedded in the spinel layers near the diopside rims (5.46–6.37 wt% MgO, 2.97–3.29 wt% TiO_2, except for one analysis with 4.01 wt% MgO and 2.14 wt% TiO_2). Only one analysis of hibonite in a spinel–pyroxene-rich inclusion
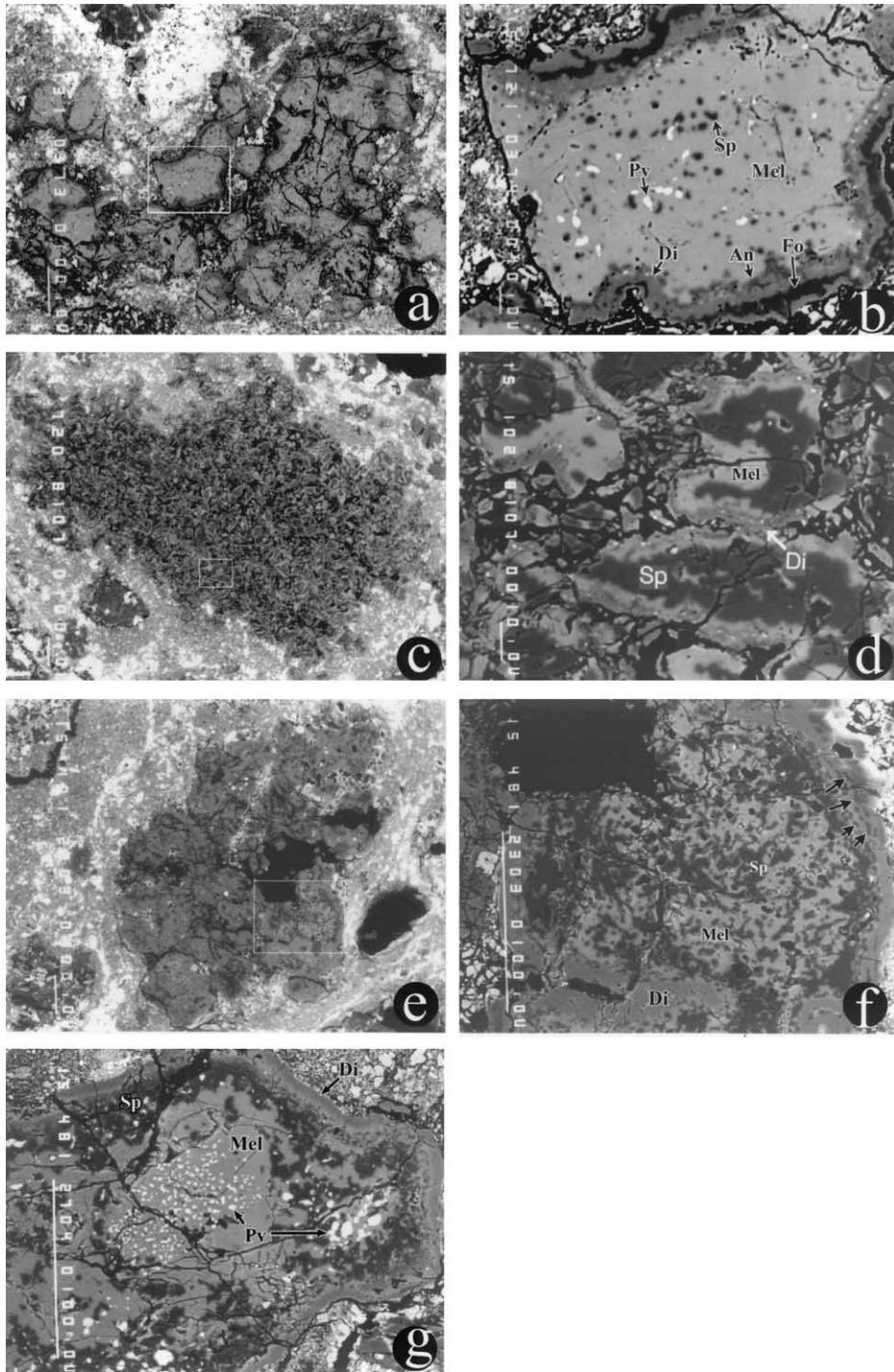
Fig. 3. BSE images of hibonite-free Type A inclusions. (a) A melilite-predominant Type A inclusion (NQJ3-5-8), consisting of several concentrically layered objects and their fragments. Width of the view is 890 μm. (b) Inset showing the concentrically zoned structure of the objects. The mineral sequence from core to rim is melilite, diopside and forsterite (Fo). Minor perovskite and spinel are enclosed in melilite, and a few anorthite (An) grains occur along the inner side of the diopside rim. The melilite in contact with the matrix is lightly altered. Width of the view is 160 μm. (c). A spinel-predominant Type A inclusion (NQW 1-7), containing lots of small and concentric objects. Width of the view is 1.47 mm. (d) The inset of the individual objects, consisting of a spinel core surrounded by a melilite layer and a diopside rim. Some grains of melilite are also enclosed in the spinel core, and fine grains of perovskite occur mainly close to the rims. Width of the view is 110 μm. (e). A diopside-rich Type A inclusion (NQL2-3-3), consisting of several concentric objects. Most of them are diopside rich, except for one is melilite–spinel–rich. Width of the view is 1.0 mm. (f). Inset showing the melilite–spinel–rich object, consisting of a core of melilite and spinel and a rim of diopside. The dark elongated grains (pointed by arrows) inside the diopside rim are forsterite. Width of the view is 240 μm. (g). A compact Type A inclusion (NQL2-7-4), showing concentric structure, with a mineral sequence of melilite, spinel and diopside outward. Perovskite is mainly enclosed in melilite. Width of the view is 246 μm.
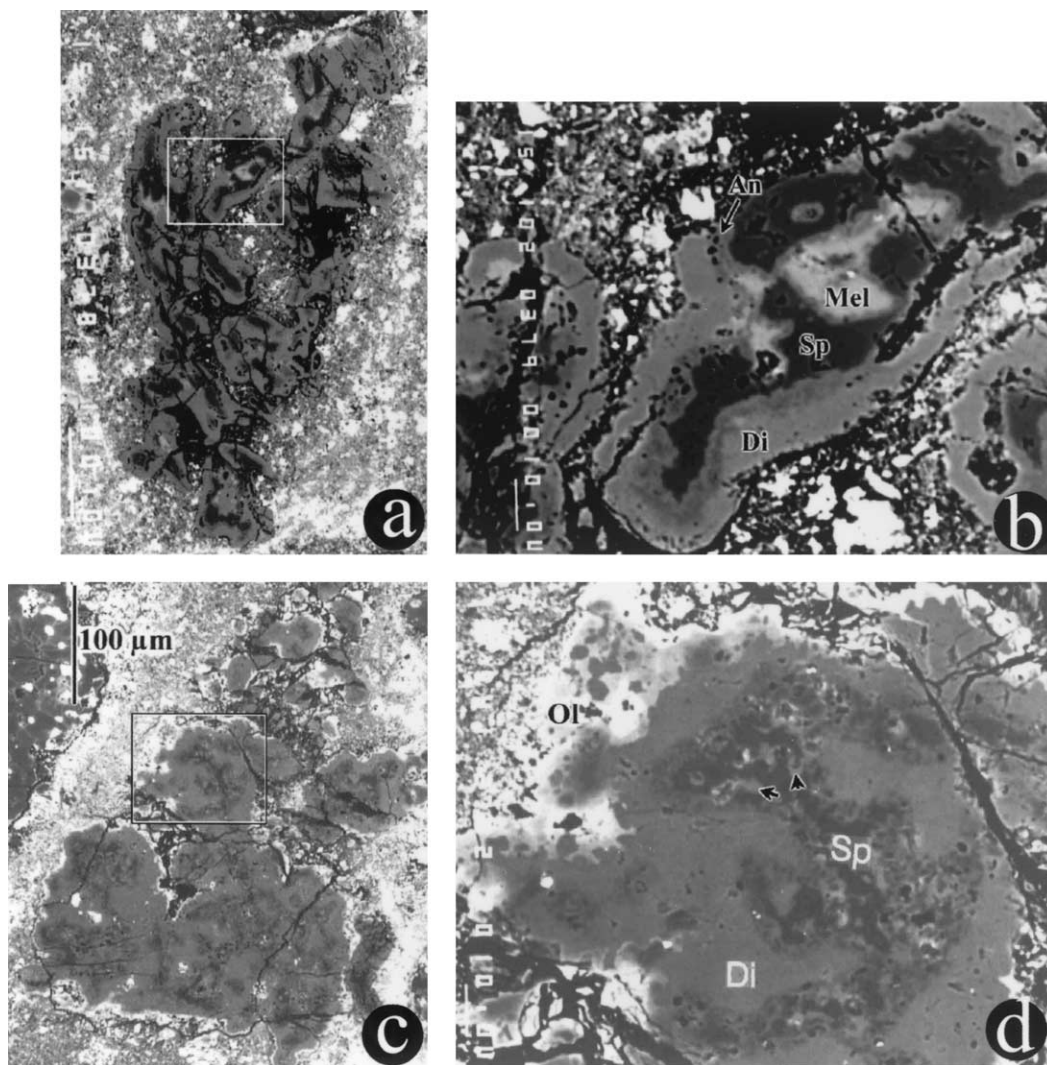
Fig. 4. BSE images of spinel–pyroxene inclusions, showing variable modal abundances of the constituents. (a) A typical spinel–pyroxene inclusion (NQJ3-5-11) consists of many concentric objects. Width of the view is 390 μm. (b) The inset shows a single concentric object, with the mineral sequence of melilite, spinel and diopside from core to rim. Minor anorthite occurs at the boundary of melilite and the inner side of the diopside rim. Width of the view is 120 μm. (c) A spinel–pyroxene inclusion (NQL2-7-2), consisting of several diopside-rich objects. Width of the view is 360 μm. (d). An enlarged image of a single object, consisting of a narrow spinel core and relatively thick rim of diopside. Minor anorthite occurs along the inner side the diopside rim, and the light gray (pointed by arrows) in spinel is melilite. Width of the view is 120 μm.

(NQL2-3-8) is available, and it contains the lowest MgO (1.46 wt%) and TiO_2 (2.52 wt%), except for another grain in CTA NQJ3-5-7 (1.17 wt% MgO, 1.45 wt% TiO_2). No hibonites contain significant Ti^{3+}, based on the stoichiometry. Representative compositions of hibonite are listed in Table 2.

3.2.2. Melilite

All melilite is gehlenitic ($Åk_{0-30}$, except for 4 analyses out of a total of 297 with $Åk_{30-40}$). Figure 7 shows the distribution patterns of åkermanite contents of melilite in the hibonite-bearing and hibonite-free Type As; melilite is significantly more gehlenitic in the former (av. $Åk_{3.9\pm3.4}$) than in the latter (av. $Åk_{11.3\pm6.9}$). However, there is no difference between the compositions of melilite in the compact vs. fluffy type A

inclusions. In addition, analyses of melilite in each CAI are heterogeneous (the range of åkermanite content is >10 mol%), but is usually not related to distance from the rims of the CAIs. Only a few grains of melilite in the spinel–pyroxene inclusions are large enough to be analyzed quantitatively, and their compositions ($Åk_{0.7-18.7}$) are indistinguishable from those of the hibonite-free Type As. Minor Na_2O (<0.68 wt%) and FeO (<1.82 wt%) were detected, and appear to be correlated to each other, suggesting that they probably come from very fine grains of secondary alteration (e.g., feldspathoids and hedenbergite) of melilite. Table 3 shows representative compositions of melilite.

3.2.3. Spinel

High FeO content (>5 wt%) of spinel is confined to significantly altered CAIs and grains near rims or fractures in the
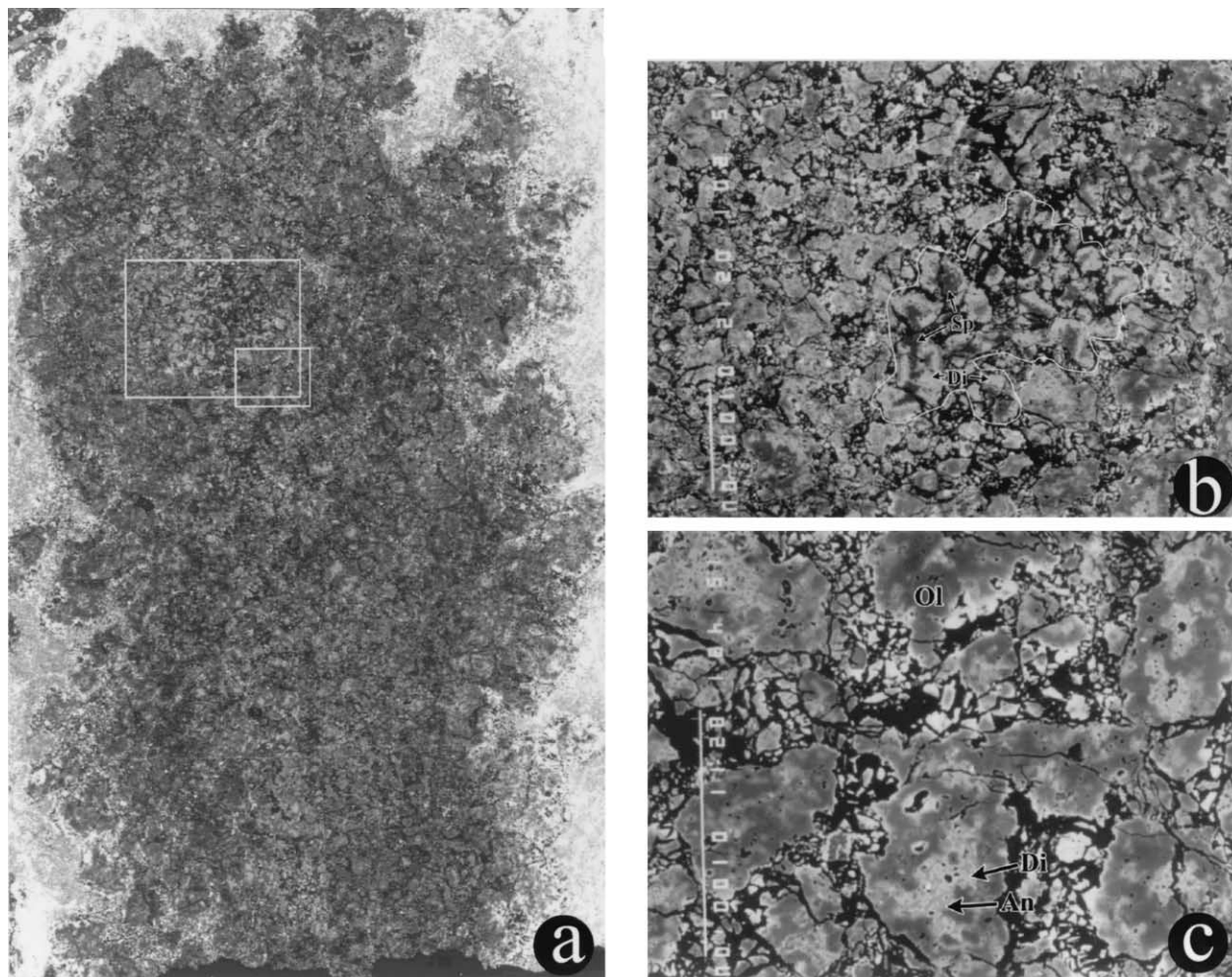
Fig. 5. (a) Photomosaic of a spinel-bearing AOA (NQJ3-3-2), width of the view is 1.8 mm. (b) The larger inset, consisting of concentric spinel-diopside objects (outlined). Width of the view is 600 μm. (c) The smaller inset, showing the occurrence of diopside and anorthite in the core of individual olivine assemblages. Note subhedral diopside grains and interstitial anorthite. Width of the view is 240 μm.

inclusions. However, some fragments of CAIs have spinel in contact with the clastic matrix, and FeO contents as low as 0.4 wt%. FeO-rich spinels are usually ZnO-bearing, and the contents of ZnO and FeO are positively correlated (Fig. 8). In addition, the FeO-rich spinels in the hibonite-bearing FTA, NQJ3-3-4, are unusually ZnO-rich relative to the spinel in other CAIs (Fig. 8). Most spinel contains low V_2O_3 (0.1–0.6 wt%), except for that in two FTAs (0.7–0.8 wt%, Table 4). The Cr_2O_3 content tends to be lower in FTAs (average is 0.09 wt% for hibonite-bearing, and 0.15 wt% for hibonite-free) than in spinel–pyroxene inclusions (av. 0.39 wt%). In addition, some diopside-rich spinel–pyroxene inclusions contain Cr_2O_3-rich spinel (0.7–2.1 wt%). Spinel in the refractory AOAs is FeO-poor, and contains lower V_2O_3 and higher Cr_2O_3 than spinel from other CAIs in the same meteorite (Table 4).

3.2.4. Ca-Pyroxene

Except for a few grains of the highly Ti/Al/Sc/V-rich clinopyroxene enclosed in melilite in three CTAs described ear-

lier (Lin et al., 2003), all Ca-pyroxenes in the other CAIs occur as rims on inclusions or on the concentric objects that constitute the inclusions. The Ca-pyroxene rims are TiO_2-poor (<3 wt%), and most of them can be referred to as diopside or Al-rich diopside (Al_2O_3 < 15 wt%). Analyses of several thick diopside rims show a decrease of Al_2O_3 and TiO_2 from the inside to the outside of the rims (Table 5).

3.2.5. Other Phases

Grossite is almost pure $CaAl_4O_7$ (Table 2). Perovskite contains minor V_2O_3 (<0.51 wt%), Al_2O_3 (0.17–0.79 wt%) and ZrO_2 (<0.28 wt%), with little Sc_2O_3 (Table 2).

4. DISCUSSION

4.1. Continuous Condensation

4.1.1. Formation of Type A inclusions

As depicted above, most Type A inclusions in Ningqiang are fluffy aggregates of concentric objects, with the clastic mate-
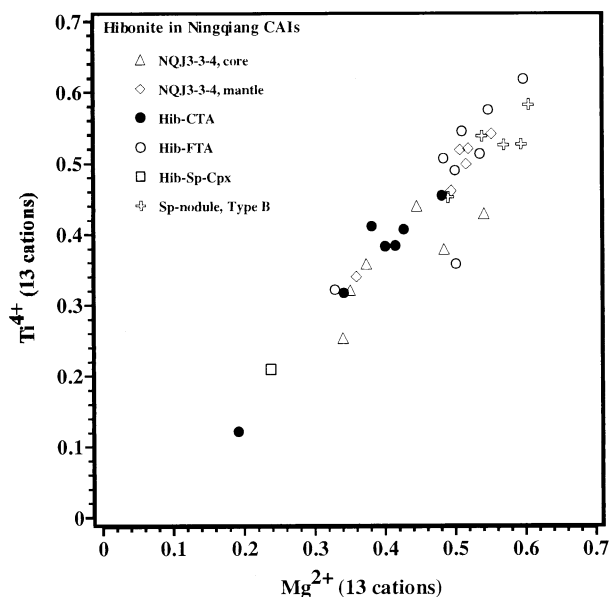
Fig. 6. Plot of Ti^{4+}-Mg^{2+} in hibonite from Ningqiang CAIs. Hibonite in the core of NQJ3-3-4 contains lower Ti^{4+} and Mg^{2+} than the laths in the mantle.
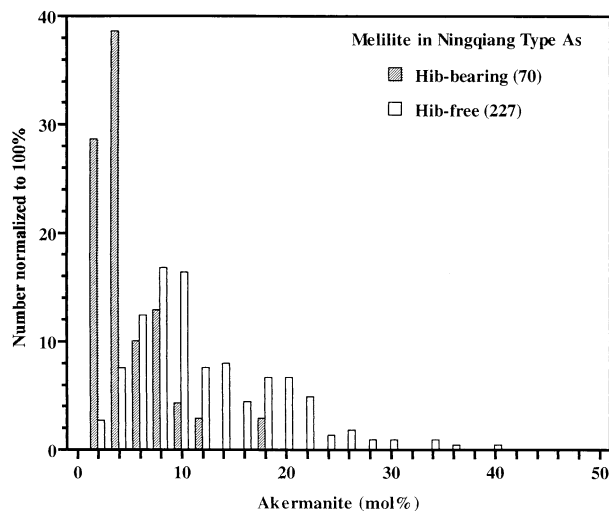

Fig. 7. Åkermanite contents of melilite in Type A inclusions from Ningqiang. Melilite in the hibonite-bearing Type As is more Al-rich than that in the hibonite-free ones.

rials filling the interstitial spaces. The fluffy structures and highly irregular shapes argue against crystallization from liquids. In fact, these fluffy Type As, including hibonite-bearing and hibonite-free, are identical to their counterparts in the Allende CV3 chondrite, which are thought to be assemblages of

nebular (gas-solid) condensates (MacPherson and Grossman, 1984). Although many fluffy Type As from Ningqiang contain low abundances of melilite and high amounts of diopside, their concentric zoning structures and mineral sequences from core to rim are the same as the melilite-predominant ones, and there is no clear gap between melilite-predominant and melilite-poor end members. In addition, as noted above, the low abundances of melilite in the fluffy Type As are partially due to the

Table 2. Representative compositions of hibonite, grossite and perovskite in Ningqiang CAIs (wt%).[a]

	Hibonite							Grossite			Perovskite	
	1	2	3	4	5[b]	6[c]	7	8	9[b]	10[d]	11	12
SiO_2	0.05	b.d.	0.07	0.07	0.14	0.07	0.09	0.05	b.d.	b.d.	0.11	0.22
TiO_2	4.28	5.34	4.57	3.85	3.05	6.22	2.52	0.07	b.d.	b.d.	56.5	56.3
Al_2O_3	85.2	82.8	85.2	86.3	87.0	82.2	87.9	77.5	79.0	78.9	0.46	0.72
V_2O_3	0.02	0.20		0.24	0.06	0.38	b.d.	b.d.	b.d.	b.d.	0.27	0.25
FeO	0.33	b.d.	0.14	0.27	0.09	0.05	0.68	b.d.	b.d.	b.d.	0.11	
MgO	3.03	2.86	2.50	1.99	2.06	3.03	1.46	0.09	0.06	0.04	0.04	b.d.
CaO	8.17	8.37	8.28	8.37	8.55	8.36	8.50	21.4	21.6	21.7	40.6	40.7
Sc_2O_3											0.14	0.07
ZrO_2											0.30	0.12
Total	101.03	99.59	100.73	101.06	100.95	100.31	101.15	99.04	100.73	100.68	98.53	98.40
					Cations per unit formula							
Si	0.005	0.000	0.008	0.007	0.017	0.007	0.010	0.003	0.000	0.000	0.003	0.005
Ti	0.359	0.454	0.384	0.321	0.254	0.525	0.209	0.003	0.001	0.001	0.977	0.972
Al	11.174	11.044	11.198	11.305	11.389	10.907	11.446	3.990	3.999	3.997	0.012	0.020
V	0.002	0.019	0.000	0.021	0.005	0.033	0.000	0.000	0.000	0.000	0.005	0.005
Fe	0.031	0.000	0.013	0.026	0.009	0.005	0.062	0.000	0.001	0.001	0.002	
Mg	0.504	0.482	0.416	0.330	0.342	0.508	0.240	0.006	0.004	0.003	0.001	0.000
Ca	0.974	1.014	0.991	0.998	1.016	1.007	1.010	0.999	0.996	1.000	1.000	1.003
Sc											0.003	0.001
Zr											0.003	0.001
Sum	13.048	13.016	13.010	13.010	13.032	12.998	13.030	5.000	5.000	5.001	2.007	2.008

[a] b.d. = below the detection limits; blank = not analyzed.
[b] For NQJ3-3-4, in the inclusion center.
[c] For NQJ3-3-4, in contact with the WL rim.
[d] For NQJ3-3-4, in the mantle.

Table 3. Representative compositions of melilite in Ningqiang CAIs (wt%).[a]

	Hib-FTA		Hib-CTA		Hib-free FTA		Hib-free CTA		Sp-Px	
	1	2	3	4	5	6	7	8	9	10
SiO$_2$	23.5	21.0	21.9	22.2	23.4	25.0	25.3	24.3	24.0	22.5
TiO$_2$	b.d.	0.22	0.08	b.d.	0.05	b.d.	0.09	b.d.	b.d.	0.07
Al$_2$O$_3$	33.5	37.5	37.2	37.0	34.8	32.6	31.9	33.9	33.7	36.6
FeO	0.48	b.d.	0.19	b.d.	0.28	0.28	b.d.	b.d.	0.45	0.08
MgO	1.16	0.08	0.20	0.35	0.88	1.70	2.18	1.37	1.27	0.39
CaO	40.5	40.1	40.8	41.1	40.8	40.7	40.4	40.9	40.3	40.6
Na$_2$O	0.07	b.d.	0.04	b.d.	0.10	0.15	b.d.	b.d.	0.15	0.05
Total	99.22	98.89	100.39	100.74	100.24	100.48	99.93	100.54	99.89	100.22
					Cations per unit formula					
Si	1.083	0.968	0.994	1.007	1.063	1.136	1.153	1.100	1.098	1.023
Ti	0.000	0.008	0.003	0.000	0.002	0.000	0.003	0.001	0.000	0.003
Al	1.820	2.039	1.995	1.976	1.867	1.743	1.712	1.812	1.812	1.962
Fe	0.018	0.000	0.007	0.002	0.011	0.010	0.000	0.000	0.018	0.003
Mg	0.080	0.005	0.014	0.024	0.060	0.115	0.148	0.093	0.087	0.026
Ca	2.003	1.984	1.992	1.997	1.987	1.981	1.972	1.987	1.974	1.976
Na	0.007	0.000	0.004	0.001	0.009	0.013	0.000	0.000	0.013	0.004
Sum	5.011	5.005	5.008	5.006	5.005	4.999	4.988	4.993	5.002	4.996
Åk (mol%)	8.8	0.2	0.7	1.5	6.7	13.3	14.8	9.6	9.9	2.5

[a] b.d. = below the detection limits.

presence of diopside rims around the CAIs or their concentric objects. The diopside rims are Ti-Al-poor, and their relative abundance increases as the CAIs or the objects become smaller, since the widths of the rims are nearly constant. In contrast, in melted Type B and C inclusions, Ca-pyroxene is referred to as Ti–Al–clinopyroxene, and mainly occurs as a subliquidus phase (Wark and Lovering, 1982; Wark, 1987).

Additional evidence for gas-solid condensation of the fluffy Type As is the mineral sequence of, from core to rim, ±per-
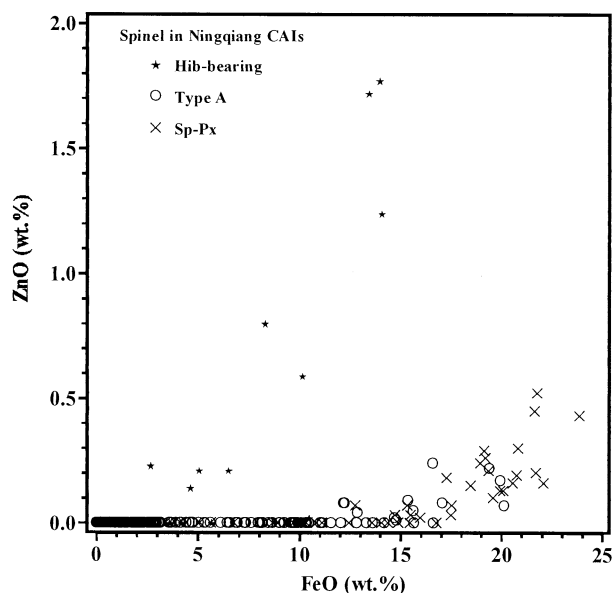

Fig. 8. Compositions of spinel in Ningqiang CAIs. FeO-rich spinels contain ZnO, and both are correlated with each other. All ZnO-rich grains labeled as hibonite (Hib)-bearing are from the inclusion NQJ3-3-4.

ovskite, ±melilite, spinel, ±melilite, and diopside. This sequence is consistent with the condensation sequence from a gas of solar composition, at $P^{tot} = 10^{-3}$ atm, as determined by condensation calculations (Yoneda and Grossman, 1995; Ebel and Grossman, 2000). The occurrence of the melilite layer surrounding spinel and/or presence of spinel in melilite, suggest formation of spinel before melilite. This is different from the calculated equilibrium condensation sequence, and is a long-standing problem (MacPherson et al., 1984, 2002). However, the observed textural relationship is not inconsistent with non-equilibrium condensation, because there is significant overlap of condensation temperature between melilite (1628–1444 K) and spinel (1501–1409 K) (Yoneda and Grossman, 1995). On the other hand, the mineral sequence mentioned above is inconsistent with the sequence expected for crystallization from a melt of fluffy Type A bulk composition. If they were melted, clinopyroxene ± anorthite would be expected to crystallize from the residual liquids, according to the phase diagram and bulk compositions of the FTAs (Fig. 9, see below). Such subliquidus clinopyroxene and/or anorthite have not been found in the FTAs. In contrast, Ca-pyroxene always occurs as the rims of the CAIs. Only a few small grains of anorthite were found in the fluffy Type As, and they coexist with other secondary alteration products replacing melilite, different from the primary grains in typical once molten CAIs of Types B and C. Furthermore, four fluffy Type A inclusions have bulk compositions that clearly plot in the forsterite field in Figure 9, hence forsterite would be expected to crystallize early from the liquids and no melilite would be expected, in contrast to observations.

According to condensation calculations for a solar gas, both hibonite and grossite condense before melilite (Ebel and Grossman, 2000). This is consistent with the occurrence of hibonite and grossite, both enclosed in melilite in the center of NQJ3-3-4 (Fig. 2b). The presence of some hibonite laths in the spinel

Table 4. Representative compositions of spinel in Ningqiang CAIs and AOAs (wt%).[a]

	Hib-FTA		Hib-CTA		Hib-free FTA		Hib-free CTA		Sp-Px			AOA	
	1	2	3	4	5	6	7	8	9[b]	10	11	12	13
SiO_2	b.d.	b.d.	b.d.	b.d.	b.d.	b.d.	b.d.	b.d.	0.06	b.d.	b.d.	b.d.	b.d.
TiO_2	0.20	0.03	0.08	0.15	0.32	0.15	0.15	0.14	0.04	0.14	b.d.	0.19	0.04
Al_2O_3	70.5	66.7	70.9	71.3	70.3	71.8	70.7	71.8	64.9	71.6	63.0	70.8	71.8
Cr_2O_3	0.04	b.d.	0.08	b.d.	0.10	0.03	0.03	0.05	0.06	0.72	0.41	0.63	0.55
V_2O_3	0.72	0.09	0.19	0.17	0.79	0.18	0.41	0.48	b.d.	0.07	0.22	0.20	0.03
FeO	0.07	13.4	4.21	0.58	2.93	0.29	2.79	0.35	18.5	0.63	21.6	1.36	0.51
MnO	b.d.	0.07	b.d.	b.d.	b.d.	b.d.	b.d.	b.d.	b.d.	b.d.	b.d.	b.d.	b.d.
MgO	27.7	17.9	26.4	28.5	25.9	28.9	26.2	28.1	15.2	28.2	12.9	27.2	28.2
CaO	0.12	0.17	0.16	0.03	0.10	0.04	0.17	0.14	0.08	0.05	0.09	0.12	0.09
ZnO	b.d.	1.72	b.d.	b.d.	b.d.	b.d.	b.d.	b.d.	0.15	b.d.	0.45	b.d.	b.d.
Total	99.33	100.06	101.95	100.78	100.44	101.41	100.39	101.13	98.93	101.41	98.71	100.48	101.15
					Cations per unit formula								
Si	0.000	0.000	0.000	0.000	0.000	0.000	0.000	0.000	0.002	0.000	0.000	0.000	0.000
Ti	0.004	0.001	0.002	0.003	0.006	0.003	0.003	0.003	0.001	0.003	0.001	0.004	0.001
Al	1.987	1.996	1.981	1.984	1.985	1.982	1.992	1.989	1.997	1.982	1.982	1.983	1.988
Cr	0.001	0.000	0.002	0.000	0.002	0.001	0.001	0.001	0.002	0.014	0.009	0.012	0.011
V	0.014	0.002	0.004	0.003	0.015	0.004	0.008	0.009	0.000	0.002	0.005	0.004	0.001
Fe	0.002	0.285	0.084	0.012	0.059	0.006	0.056	0.007	0.403	0.013	0.483	0.027	0.010
Mn	0.000	0.002	0.000	0.000	0.000	0.001	0.000	0.000	0.000	0.001	0.000	0.000	0.000
Mg	0.986	0.678	0.932	1.003	0.925	1.009	0.934	0.986	0.591	0.985	0.512	0.966	0.988
Ca	0.003	0.005	0.004	0.001	0.003	0.001	0.005	0.004	0.002	0.001	0.003	0.003	0.002
Zn	0.000	0.033	0.000	0.000	0.000	0.000	0.000	0.000	0.003	0.000	0.009	0.000	0.000
Sum	2.996	3.001	3.006	3.004	2.994	3.005	2.998	2.999	2.997	2.997	3.002	2.998	3.000

[a] b.d. = below the detection limits.
[b] Hibonite-bearing.

layer in NQL1-4-1 cannot be explained by equilibrium condensation (Yoneda and Grossman, 1995; Ebel and Grossman, 2000). One possibility is non-equilibrium condensation, as indicated by the concentric structures of the CAIs or their individual objects. During non-equilibrium processes, earlier condensates may be covered by the successive phases, and protected from reaction with the gas, as proposed by Petaev and Wood (1998). Another possibility is that the laths of hibonite in

Table 5. Representative compositions of Ca-pyroxene in Ningqiang CAI rims (wt%).[a]

	Hib-FTA		Hib-CTA		Hib-free FTA		Hib-free CTA		Sp-Px		AOA	
	1	2	3	4[b]	5[c]	6	7	8	9	10	11
SiO_2	55.3	54.4	54.8	44.9	55.7	53.8	55.2	53.9	55.7	55.7	54.1
TiO_2	b.d.	0.12	0.06	2.29	0.28	0.43	0.11	0.32	0.03	0.08	0.54
Al_2O_3	0.45	2.79	2.28	14.9	0.78	2.82	0.76	2.19	1.09	0.71	2.05
Cr_2O_3	b.d.	b.d.	b.d.	0.28	0.12	0.17	b.d.	0.11	b.d.	b.d.	b.d.
FeO	0.52	0.50	0.15	0.25	0.37	0.46	0.34	0.47	b.d.	0.36	0.20
MnO	b.d.	b.d.	b.d.	b.d.	0.06	b.d.	b.d.	b.d.	b.d.	b.d.	b.d.
MgO	18.1	18.7	17.2	16.2	19.1	17.3	18.2	17.2	19.2	18.6	19.1
CaO	25.8	24.4	26.5	22.4	25.1	25.5	25.7	25.9	24.8	25.3	23.7
Na_2O	b.d.	b.d.	b.d.	b.d.	b.d.	b.d.	b.d.	b.d.	b.d.	b.d.	b.d.
Total	100.10	100.96	100.98	101.36	101.53	100.60	100.23	100.13	100.87	100.71	99.68
				Cations per unit formula							
Si	1.993	1.938	1.957	1.600	1.975	1.931	1.985	1.946	1.982	1.990	1.946
Ti	0.000	0.003	0.002	0.061	0.008	0.012	0.003	0.009	0.001	0.002	0.015
Al	0.019	0.117	0.096	0.627	0.033	0.120	0.032	0.093	0.046	0.030	0.087
Cr	0.000	0.000	0.000	0.008	0.003	0.005	0.000	0.003	0.000	0.000	0.000
Fe	0.016	0.015	0.004	0.007	0.011	0.014	0.010	0.014	0.000	0.011	0.006
Mn	0.000	0.000	0.000	0.001	0.002	0.001	0.000	0.001	0.000	0.000	0.000
Mg	0.974	0.994	0.918	0.862	1.012	0.928	0.975	0.928	1.018	0.989	1.026
Ca	0.995	0.932	1.017	0.855	0.953	0.982	0.991	1.003	0.947	0.971	0.915
Na	0.000	0.000	0.000	0.001	0.002	0.001	0.000	0.001	0.000	0.000	0.000
Sum	3.997	4.000	3.993	4.021	3.997	3.992	3.996	3.996	3.994	3.993	3.994

[a] b.d. = below the detection limits.
[b] At the inner side of the rims.
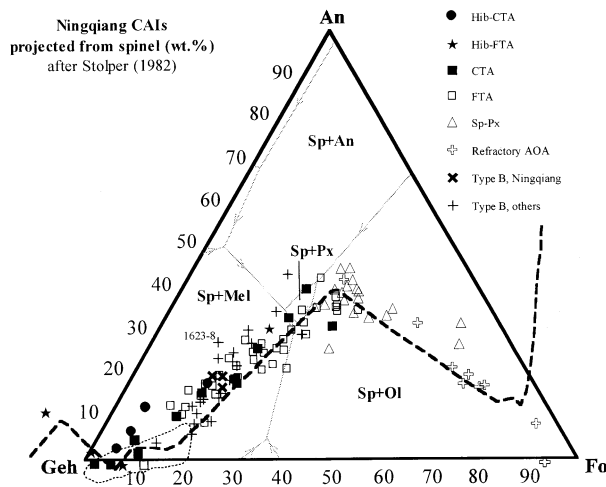[c] At the outside of the rims.

Fig. 9. Bulk compositions of Ningqiang CAIs projected from spinel onto the anorthite (An)–gehlenite (Geh)–forsterite (Fo) ternary plane. Most of the analyses plot along the condensation trajectory (dashed line), in the order hibonite-bearing Type As, Type As, spinel–pyroxene inclusions and refractory AOAs, from high to low temperature. Most Type Bs overlap with the Ningqiang Type A inclusions, that extend the range of typical Type As (dotted line) along the condensation trajectory to the middle of the chart. Other labels are: spinel (Sp), olivine (Ol), pyroxene (Px), melilite (Mel). The condensation trajectory (P = 10^{-5} bar) and range of typical Type As are from Grossman et al. (2000); data for the Type Bs: those from Ningqiang from Lin and Kimura (2000), 1623-8 from MacPherson and Davis (1993); and others from Wark and Lovering (1982).

the spinel layer might crystallize from a liquid if the inclusion was melted. However, the irregular assemblage of NQL1-4-1 that consists of several concentric objects is inconsistent with a melting origin. In addition, the high TiO_2 content of the hibonite (6–7.2 wt%) requires at least 3.6 wt% TiO_2 in the melt, based on the partition coefficient of TiO_2 between hibonite and melt (0.8–2) (Beckett and Stolper, 1994), much higher than the bulk TiO_2 concentration of the inclusion (2.0 wt%).

The gehlenitic composition of melilite in the fluffy Type As ($Åk_{0-30}$) is similar to that in their counterparts in Allende (MacPherson and Grossman, 1984), and, again, argues for gas-solid condensation of the inclusions. As mentioned above, the bulk compositions of some of the fluffy Type As from Ningqiang are rather MgO-, SiO_2-rich. Melilites with much higher contents of åkermanite would have been expected, if they crystallized from such MgO-, SiO_2-rich melts. Åkermanitic melilites ($Åk_{50-90}$) have been found in two melted Type Bs from the same meteorite (Lin and Kimura, 2000), which have bulk compositions in the range of the fluffy Type As (Fig. 9). Furthermore, the higher Al_2O_3 content of melilite in the hibonite-bearing Type As, than that in the hibonite-free ones, is also consistent with the gas-solid condensation. The hibonite-bearing Type As probably incorporated condensates formed at higher temperatures than the hibonite-free ones, since hibonite is one of the earliest condensates. During condensation, as temperature decreases melilite becomes more åkermanitic (Yoneda and Grossman, 1995).

Some of the compact Type As were probably once molten or partially molten, especially the three inclusions with highly Ti/Sc/V-rich clinopyroxene enclosed in melilite (Lin et al.,

2003) and four other compact hibonite-bearing Type As with many bubble-like voids in the melilite. Neither highly Ti, Al-rich clinopyroxene rims on perovskite, nor Sc/V-rich Ti–Al–clinopyroxene in melilite were reported in typical FTAs. In addition, their textural relationships are different from the condensation sequences of the nebula. The highly Ti, Al-rich clinopyroxene rims probably formed by reaction of preexisting perovskite with melt, and the Sc/V-rich Ti–Al–clinopyroxene may be relicts (Lin et al., 2003). However, many of the others may have experienced only annealing, instead of melting, if the heating events postdated formation of the diopside rims. Evidence against a liquid origin for these inclusions includes: (1) their highly irregular shapes, (2) the concentric structures and mineral sequences consistent with gas-solid condensation, and (3) identical mineral chemistry with the fluffy types, which are thought to be condensates. As discussed above, the presence of subliquidus Ti–Al–clinopyroxene ± anorthite, and åkermanitic compositions of melilite would be expected, at least for the MgO-, SiO_2-rich inclusions, if they crystallized from melts.

Alternatively, these compact Type A inclusions may crystallize from melts if the heating events predated formation of the diopside rims of their precursors (i.e., the proposed FTAs). In this case, bulk compositions of the precursors of CTAs are close to the gehlenite apex in Fig 9)., and gehlenitic melilite is expected from such refractory melts. The observations of CTAs are consistent with this scenario.

4.1.2. Formation of Spinel-Pyroxene inclusions

The formation of spinel–pyroxene inclusions is controversial. Abundant spinel–pyroxene inclusions were reported in the Cold Bokkeveld (CM2) chondrite (Greenwood et al., 1994), and the authors suggested that they crystallized from liquid produced by melting refractory precursors, mainly based on textural relationships and compositional trends of pyroxenes. In contrast, analyses of trace elements show heterogeneity of the REEs in such inclusions, and the REE patterns of many inclusions are inconsistent with mineral/liquid or mineral/mineral partitioning (MacPherson and Davis, 1994). Kornacki and Fegley (1984) and Kornacki and Wood (1985) suggested that spinel–pyroxene inclusions formed by melting and evaporation of primitive dust to explain the fractionation of Ca/Al in these inclusions. However, many spinel–pyroxene inclusions lack enrichment of the heavier Mg isotopes (Brigham et al., 1985; Greenwood et al., 1994; MacPherson and Davis, 1994), suggesting significant evaporation did not occur. The observations of the spinel–pyroxene inclusions from Ningqiang are also inconsistent with liquid origins. The predicted crystallization sequence, from high to low temperature, is spinel, forsterite, anorthite and/or clinopyroxene, based on their bulk compositions and the phase diagram (Fig. 9). This is different from the observed mineral assemblages and textural relationships. Although the absence of subliquidus anorthite can be related to its postponement during dynamic crystallization (Stolper and Paque, 1986), all diopside occurs as rims on the inclusions, instead of as a subliquidus phase crystallized from residual melts. In addition, much more åkermanitic melilite would be expected to crystallize from such MgO-, SiO_2-rich melts. Melting of the inclusions before formation of the diopside rims seems unlikely. If the diopside rims postdated the heating

events, precursors of the inclusions consist predominantly of spinel with minor melilite. Melting of such spinel-predominant materials requires very high temperatures (Simon et al., 1994; Lin and Kimura, 2000), again, not favoring a liquid origin.

Alternatively, many spinel–pyroxene inclusions are aggregates of vapor-solid condensates (MacPherson et al., 1983; MacPherson and Davis, 1994; Weber and Bischoff, 1997), which is supported by their fluffy textures, group II REE patterns and the Mg isotopic compositions. The petrography and mineral chemistry of the spinel–pyroxene inclusions from Ningqiang are similar to their counterparts in other carbonaceous chondrites. The spinel–pyroxene inclusions in Ningqiang lack phyllosilicates, because Ningqiang experienced different secondary alteration conditions than other carbonaceous chondrites. The loose structures of the spinel–pyroxene inclusions from Ningqiang strongly argue against crystallization from melts. Additional evidence for gas-solid condensation is the Al-rich compositions of melilite. All of the melilite analyzed is gehlenitic and compositionally similar to those in the fluffy Type As, although the bulk compositions of the spinel–pyroxene inclusions are MgO-, SiO_2-rich and CaO-poor in comparison to FTAs.

As depicted above, the concentric structures of spinel–pyroxene inclusions are similar to the fluffy Type As. Furthermore, the modal compositions of spinel–pyroxene inclusions fall along an extension of the range noted for the fluffy Type A inclusions. In particular, the melilite-bearing spinel–pyroxene inclusions are almost identical to the melilite-poor fluffy Type As, except for slightly different abundances of melilite. The order of formation for the spinel–pyroxene inclusions is ±perovskite, ±melilite, ±spinel, diopside, ±forsterite, ±diopside, based on the textural relationship of the inclusions, and is consistent with the condensation sequence (Yoneda and Grossman, 1995). The repeat sequence of diopside, forsterite, diopside is probably due to their close condensation temperatures (diopside: 1449 K; forsterite: 1443 K) (Yoneda and Grossman, 1995). In addition, the decrease of Al and Ti contents of the diopside from the inner side to the outer side of the rims is expected during condensation (Yoneda and Grossman, 1995). The general lack of melilite in spinel–pyroxene inclusions from other carbonaceous chondrites argues against equilibrium condensation (Kornacki and Fegley, 1984; Kornacki and Wood, 1985; Greenwood et al., 1994). However, this could at least partially be due to common alteration of these CAIs. The sequence of spinel predating melilite may not be a severe problem for the condensation origin of spinel–pyroxene inclusions from Ningqiang, because such a textural relationship was found in only about half of the melilite-bearing spinel–pyroxene inclusions. In contrast, the other CAIs contain melilite enclosed in and/or intergrown with spinel. This is consistent with formation of spinel–pyroxene inclusions after FTAs (see below) and significant overlapping of the condensation temperatures between melilite (e.g., 1628–1444K) and spinel (e.g., 1501–1409K).
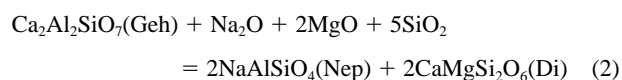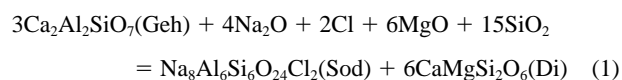
Only one of the spinel–pyroxene inclusions from Ningqiang is hibonite-bearing, and it may crystallize from liquid and/or experience significant evaporation, different from the above hibonite-free ones. The intergrowth of hibonite laths with spinel in the core and the absence of melilite and grossite cannot be explained by condensation models, since hibonite is expected to react with vapor to form grossite that continues to form melilite before condensation of spinel (e.g., Kornacki and Wood, 1984).

4.1.3. Continuous condensation of the nebula

According to condensation models, bulk compositions of vapor-solid condensates are expected to vary along the condensation trajectory shown in Figure 9. However, only a few data for Type As (mostly compact type) plot on a narrow range at the beginning of the condensation trajectory (Fig. 9). Fluffy Type As are generally referred to as aggregates of vapor-solid condensates. However, few bulk compositions of FTAs have been analyzed, mainly due to their common and heavy alteration, and complicated and loose structures with clastic matrix interstitial to the individual objects.

According to the above discussion, we argue that most CAIs from Ningqiang have not been melted, and may be the pristine assemblages of vapor-solid condensates from the solar nebula. Thus, the bulk compositions of these inclusions are expected to plot on the condensation trajectory. All analyses of the bulk compositions are listed in Table 1. Some of these contain high contents of Na_2O, FeO, and Cl, introduced by the secondary alteration. The prealteration bulk compositions of the inclusions can be calculated based on the following assumptions: (1) all Cl and a part of Na_2O occur as sodalite, (2) after subtraction of sodalite, excess Na_2O higher than 0.68 wt% (the maximum Na_2O content of melilite) is contributed by nepheline, (3) most FeO is introduced by replacing MgO in spinel and/or olivine. Because reaction of melilite with vapor to produce feldspathoids and diopside is the most common alteration of Ningqiang CAIs, and all melilites are gehlenitic, the prealteration bulk compositions can be calculated using reactions 1 and 2 below:

$$3Ca_2Al_2SiO_7(Geh) + 4Na_2O + 2Cl + 6MgO + 15SiO_2$$
$$= Na_8Al_6Si_6O_{24}Cl_2(Sod) + 6CaMgSi_2O_6(Di) \quad (1)$$

$$Ca_2Al_2SiO_7(Geh) + Na_2O + 2MgO + 5SiO_2$$
$$= 2NaAlSiO_4(Nep) + 2CaMgSi_2O_6(Di) \quad (2)$$

Minor hedenbergite is neglected for simplification, and it does not change the result if we plot the bulk compositions in the spinel-projected gehlenite–anorthite– forsterite ternary diagram and take the above assumption that all FeO is introduced by substituting MgO. Wollastonite is not considered here, because it is less common. Figure 9 shows the prealteration bulk compositions of all CAIs analyzed in this work. Three conclusions can be made based on this figure: (1) The bulk compositions of most CAIs are consistent with the condensation trajectory. (2) There is significant overlap among the various types of the CAIs. (3) Hibonite-bearing Type As (except for two analyses) plot at the beginning of the trajectory, followed by hibonite-free Type As, and then by spinel–pyroxene inclusions. Analyses of the refractory AOAs are also plotted for comparison. They overlap with the spinel–pyroxene inclusions, and are close to the condensation trajectory at the lower temperature range. The coincidence of the bulk compositions of the CAIs with the predicted condensation trajectory is consistent with the proposed condensation origin of these assemblages, and in the case

of the spinel–pyroxene inclusions, argues against significant evaporation during their formation (Kornacki and Fegley, 1984; Kornacki and Wood, 1985).

Many studies of AOAs from other carbonaceous chondrites illustrate that these objects are vapor-solid condensate aggregates (e.g., Grossman and Steele, 1976; Komatsu et al., 2001). Although some of the refractory AOAs from Ningqiang probably experienced annealing events, none of them show evidence for crystallization from melts. The discovery of refractory AOAs from Ningqiang, especially the spinel-bearing AOAs, makes a genetic linkage between spinel–pyroxene inclusions and AOAs, with regard to their continuous bulk and modal compositions and textural relationships. Other evidences for a genetic relationship between AOA and CAIs are: (1) quantities of refractory components (i.e., CAI-regions) in AOAs are continuously distributed from 0 to 100% as modal proportion (Itoh et al., 2002); (2) All major components of AOAs are enriched in ^{16}O similar to CAIs (Fagan et al., 2002; Itoh et al., 2002); (3) the AOAs contain radiogenic ^{26}Mg with an inferred initial ^{26}Al/^{27}Al of 2.7–3.2 $\times$ 10^{-5} (Itoh et al., 2002), compatible to CAIs. Thus, the petrography, mineral chemistry, oxygen isotopes and Al-Mg isotopic system strongly indicate a genetic relationship between CAIs and AOAs.

4.2. Precursors of Type B Inclusions

Melilite–Ti–Al–clinopyroxene–rich inclusions (Type B) are the most common coarse-grained CAIs in CV3 chondrites and have been extensively studied. However, the precursors of Type Bs are controversial. It is generally suggested that Type Bs are evaporation residues of Mg-, Si-rich materials (Wark and Lovering, 1982). This is supported by recent computation of non-equilibrium evaporation, which reproduces the bulk compositions of Type Bs by evaporating MgO and SiO$_2$ from possible condensate assemblages as the starting materials (Grossman et al., 2000). However, the proposed MgO-, SiO$_2$-rich precursor materials have not yet been related to any assemblages found in carbonaceous chondrites. Condensation calculations for a nebular gas with high dust/gas ratios or under high pressures predict the existence of non-ideal CaO-MgO-Al$_2$O$_3$-SiO$_2$ (CMAS) liquids that have bulk compositions overlapping with some Type Bs (Yoneda and Grossman, 1995). Some Type Bs could crystallize from the CMAS liquids, but many others are not explained (see figs. 21 and 22, Yoneda and Grossman, 1995). In addition, condensation of the CMAS liquids requires extreme conditions for which there is little evidence.

We note in Figure 9 that the bulk compositions of most Type Bs overlap with those of the Type A inclusions from Ningqiang. These Type B inclusions could have crystallized from liquids produced by melting the Type As without significant evaporation, indicating that such Type A inclusions are possible precursors of Type Bs. In addition, åkermanitic melilite is expected to crystallize from MgO-, SiO$_2$-rich molten fluffy Type A inclusions, consistent with the observation of Type Bs. The two Type Bs from Ningqiang plot in the range of Type As, and they show no mass fractionation with ^{25}Mg-enrichment (Lin et al., 2000).

A few of the Type Bs show deviation from the range of the Type A inclusions, and they all shift toward the direction of less MgO and/or SiO$_2$ (Fig. 9). One possibility is that the precursor condensates of these inclusions have not been sampled in this work. However, this is unlikely because the Type As from Ningqiang plot on or close to the condensation trajectory. Another possibility is that these Type B inclusions are anorthite-bearing and may require melting of Type As with melilite significantly replaced by anorthite. Such a process could be related to the deviation of bulk compositions of some Type A inclusions from the predicted condensation trajectory. However, it is unlikely that more altered anorthite-bearing Type A inclusions were selectively melted to form Type Bs. Alternatively, these Type B inclusions may have experienced significant evaporation and lost some MgO $\pm$ SiO$_2$, during melting of the precursor Type As. Evaporation during formation of some CAIs and chondrules have been confirmed by enrichment of heavy isotopes of Mg and Si (e.g., Galy et al., 2000; Grossman et al., 2000). This scenario is consistent with all of these Type B inclusions plotting above the compositional range of Type As, because evaporative loss of MgO $\pm$ SiO$_2$ will move the bulk compositions of the precursor materials toward a direction away from the forsterite apex in the diagram. One of these Type B2 inclusions, 1623-8 from the Vigarano CV3 chondrite, which shows the largest deviation from the compositional trend of the Ningqiang Type As, has significant mass fractionation of Mg (F_{Mg} = 9.9) (Loss et al., 1994) and Si (F_{Si} = 4.9) (Clayton et al., 1987), consistent with evaporation of its precursor material.

5. CONCLUSIONS

We have studied a number of CAIs from the Ningqiang carbonaceous chondrite that may be referred to as hibonite-bearing or hibonite-free Type As and spinel–pyroxene inclusions. Many of them are loose (fluffy) assemblages of concentrically layered objects, which have mineral sequences, from core to rim, that are consistent with condensation from the nebula. Modal compositions of the three types are continuous, without a clear gap between them. In addition, 9 refractory AOAs contain spinel $\pm$ diopside $\pm$ anorthite in the centers of the aggregates, which are similar to spinel–pyroxene inclusions. All melilites in the CAIs are gehlenitic (Åk$_{<30}$). It is proposed that the hibonite-bearing FTAs, hibonite-free FTAs, spinel–pyroxene inclusions and refractory AOAs form a continuous series of gas-solid condensates that formed as nebular temperatures decreased. Although some CTAs may have been molten, others probably experienced only solid-state recrystallization.

The bulk compositions of the CAIs plot along the condensation trajectory for the solar nebula. Hibonite-bearing Type As tend to sample gas-solid condensates at high temperatures, followed by hibonite-free Type As, and then by spinel–pyroxene inclusions. Bulk compositions of the refractory AOAs are close to the trajectory at lower temperatures. It is noteworthy that the bulk compositions of most Type B inclusions are similar to those of Type As from the Ningqiang meteorite. These Type Bs may have crystallized from liquids produced by melting of Type As, without significant evaporation. A few Type Bs show deviation from the bulk compositions of Type As, and probably experienced significant evaporation.

Associate editor: S. Russell

REFERENCES

Albee A. L., Quick J. E., and Chodos A. A. (1977) Source and magnitude of errors in "broad-beam analysis" (BDA) with the electron probe (abstract). *Lunar Planet. Sci.* **8,** 7–9.

Beckett J. R. and Grossman L. (1988) The origin of type C inclusions from carbonaceous chondrites. *Earth Planet. Sci. Lett.* **89,** 1–14.

Beckett J. R. and Stolper E. (1994) The stability of hibonite, melilite and other aluminous phases in silicate melts: Implications for the origin of hibonite-bearing inclusions from carbonaceous chondrites. *Meteoritics* **29,** 41–65.

Beckett J. R., Simon S. B., and Stolper E. (2000) The partitioning of Na between melilite and liquid: Part II. Applications to Type B inclusions from carbonaceous chondrites. *Geochim. Cosmochim. Acta* **64,** 2519–2534.

Brigham C. A., Papanastassiou D. A., and Wasserburg G. J. (1985) Mg isotopic heterogeneities in fine-grained Ca-Al inclusions (abstract). *Lunar Planet. Sci.* **16,** 93–94.

Clayton R. N., Mayeda T. K., MacPherson G. J., and Grossman L. (1987) Oxygen and silicon isotopes in inclusions and chondrules from Vigarano (abstract). *Lunar Planet. Sci.* **18,** 185–186.

Ebel D. S. and Grossman L. (2000) Condensation in dust-enriched systems. *Geochim. Cosmochim. Acta* **64,** 339–366.

Fagan T. J., Yurimoto H., Krot A. N., and Keil K. (2002) Constraints on oxygen isotopic evolution from an amoeboid olivine aggregate and Ca, Al-rich inclusion from the CV3 Efremovka (abstract). *Lunar Planet. Sci.* **33,** 1507.

Galy A., Young E. D., Ash R. D., and O'Nions R. K. (2000) The formation of chondrules at high gas pressures in the solar nebula. *Science* **290,** 1751–4.

Greenwood R. C., Lee M. R., Hutchison R., and Barber D. J. (1994) Formation and alteration of CAIs in Cold Bokkeveld (CM2). *Geochim. Cosmochim. Acta* **58,** 1913.

Grossman L. (1975) Petrography and mineral chemistry of Ca-rich inclusions in the Allende meteorite. *Geochim. Cosmochim. Acta* **39,** 433–454.

Grossman L. and Ganapathy R. (1975) Volatile elements in Allende inclusions. *Proc. Lunar Sci. Conf.* **6,** 1729–1736.

Grossman L. and Ganapathy R. (1976) Trace elements in the Allende meteorite: II—Fine-grained, Ca-rich inclusions. *Geochim. Cosmochim. Acta* **40,** 967–977.

Grossman L. and Steele I. M. (1976) Amoeboid olivine aggregates in the Allende meteorite. *Geochim. Cosmochim. Acta* **40,** 149–155.

Grossman L., Ebel D. S., Simon S. B., Davis A. M., Richter F. M., and Parsad N. M. (2000) Major element chemical and isotopic compositions of refractory inclusions in C3 chondrites: The separate roles of condensation and evaporation. *Geochim. Cosmochim. Acta* **64,** 2879–2894.

Ikeda Y. (1980) Petrology of Allan Hills-764 chondrite (LL3). *Mem. NIPR Res. Spec. Issue.* **17,** 50–82.

Itoh S., Rubin A. E., Kojima H., Wasson J. T., and Yurimoto H. (2002) Amoeboid olivine aggregates and AOA-bearing chondrule from Y-81020 CO3.0 chondrite: Distribution of oxygen and magnesium isotopes (abstract). *Lunar Planet. Sci.* **33,** 1490.

Kallemeyn G. W., Rubin A. E., and Wasson J. T. (1991) The compositional classification of chondrites: V. The Karoonda (CK) group of carbonaceous chondrites. *Geochim. Cosmochim. Acta* **55,** 881–892.

Kimura M., Noguchi T., Lin Y., and Wang D. (1996) Petrology and mineralogy of an unusual Ningqiang carbonaceous chondrite. In *Geochemical Studies on Synthetic and Natural Rock Systems* (eds. A. K. Gupta, K. Onuma, and M. Arima), pp. 153–165. Allied.

Komatsu M., Krot A. N., Petaev M. I., Ulyanov A. A., Keil K., and Miyamoto M. (2001) Mineralogy and petrography of amoeboid olivine aggregates from the reduced CV3 chondrites Efremovka, Leoville and Vigarano: Products of nebular condensation, accretion and annealing. *Meteorit. Planet. Sci.* **36,** 629–641.

Kornacki A. S. and Fegley B. Jr. (1984) Origin of spinel-rich chondrules and inclusions in carbonaceous and ordinary chondrites. *Proc. Lunar Planet. Sci. Conf.* **15**(89), B588–B596.

Kornacki A. S. and Wood J. A. (1984) Petrography and classification of Ca, Al-rich and olivine-rich inclusions in the Allende CV3 chondrite. *J. Geophys. Res. Suppl.* **89,** B573–B587.

Kornacki A. S. and Wood J. A. (1985) Mineral chemistry and origin of spinel-rich inclusions in the Allende CV3 chondrite. *Geochim. Cosmochim. Acta* **49,** 1219–1237.

Lin Y. and Kimura M. (1997a) Titanium-rich oxides bearing plagioclase–olivine inclusions in the unusual Ningqiang carbonaceous chondrite. *Antarct. Meteorite Res.* **10,** 227–248.

Lin Y. and Kimura M. (1997b) Calcium–aluminum–rich inclusions of the Ningqiang carbonaceous chondrite: Prototype of the solar nebular condensates and possible precursors of Type B inclusions (abstract). *Meteorit. Planet. Sci.* **32,** A80.

Lin Y. and Kimura M. (1998) Anorthite–spinel–rich inclusions in the Ningqiang carbonaceous chondrite: Genetic links between inclusions of Types A and C. *Meteorit. Planet. Sci.* **33,** 435–446.

Lin Y. and Kimura M. (2000) Two unusual type B inclusions in the Ningqiang carbonaceous chondrite: Evidence for relicts, xenoliths and multi-heating. *Geochim. Cosmochim. Acta* **64,** 4031–4047.

Lin Y., Floss C., Stadermann F. J., Zinner E., and Kimura M. (2000) Isotopic and trace element compositions of two unusual type B inclusions from the Ningqiang carbonaceous chondrite (abstract). *Lunar Planet. Sci.* **31,** 1624.

Lin Y., Kimura M., and Wang D. (2003) Fassaites in compact Type A Ca-Al–rich inclusions in the Ningqiang carbonaceous chondrite: Evidence for heating event in the nebula. *Meteorit. Planet. Sci.,* in press.

Loss R. D., Lugmair G. W., Davis A. M., and MacPherson G. J. (1994) Isotopically distinct reservoirs in the solar nebula: Isotope anomalies in Vigarano meteorite inclusions. *Astrophys. J.* **436,** L193–L196.

MacPherson G. J. and Grossman L. (1981) A once-molten, coarse-grained, Ca-rich inclusion in Allende. *Earth Planet. Sci. Lett.* **52,** 16–24.

MacPherson G. J., Bar-Matthews M., Tanaka T., Olsen E., and Grossman L. (1983) Refractory inclusions in the Murchison meteorite. *Geochim. Cosmochim. Acta* **47,** 823–839.

MacPherson G. J. and Grossman L. (1984) "Fluffy" Type A Ca-, Al-rich inclusions in the Allende meteorite. *Geochim. Cosmochim. Acta* **48,** 29–46.

MacPherson G. J., Grossman L., Hashimoto A., Bar-Matthews M., and Tanaka T. (1984) Petrographic studies of refractory inclusions from the Murchison meteorite. *J. Geophys. Res. Suppl.* **89,** C299–C312.

MacPherson G. J. and Davis A. M. (1993) A petrologic and ion microprobe study of a Vigarano Type B refractory inclusion: Evolution by multiple stages of alteration and melting. *Geochim. Cosmochim. Acta* **57,** 231–243.

MacPherson G. J. and Davis A. M. (1994) Refractory inclusions in the prototypical CM chondrite, Mighei. *Geochim. Cosmochim. Acta* **58,** 5599–5625.

MacPherson G. J., Krot A. N., Ulyanov A. A., and Hicks T. (2002) A comprehensive study of pristine, fine-grained, spinel-rich inclusions from the Leoville and Efremovka CV3 chondrites, I: Petrology (abstract). *Lunar Planet. Sci.* **33,** 1526.

Mason B. and Taylor S. R. (1982) Inclusions in the Allende meteorite. *Smiths. Contrib. Earth Sci.* **25,** 30.

Petaev M. I. and Wood J. A. (1998) The condensation with partial isolation (CWPI) model of condensation in the solar nebula. *Meteorit. Planet. Sci.* **33,** 1123–1137.

Podosek F. A., Zinner E. K., MacPherson G. J., Lundberg L. L., Brannon J. C., and Fahey A. J. (1991) Correlated study of initial $^{87}Sr/^{86}Sr$ and Al/Mg isotopic systematics and petrologic properties in a suite of refractory inclusions from the Allende meteorite. *Geochim. Cosmochim. Acta* **55,** 1083–1110.

Rubin A. E., Wang D., Kallemeyn G. W., and Wasson J. T. (1988) The Ningqiang meteorite: Classification and petrology of an anomalous CV chondrite. *Meteoritics* **23,** 13–23.

Simon S. B., Yoneda S., Grossman L., and Davis A. M. (1994) A $CaAl_4O_7$-bearing refractory spherule from Murchison: Evidence for very high-temperature melting in the solar nebula. *Geochim. Cosmochim. Acta* **58,** 1937–1949.

Simon S. B., Davis A. M., and Grossman L. (1999) Origin of compact type A refractory inclusions from CV3 carbonaceous chondrites. *Geochim. Cosmochim. Acta* **63,** 1233–1248.

Simon S. B., Grossman L., Krot A. N., and Ulyanov A. A. (2002) Bulk chemical compositions of Type B refractory inclusions (abstract). *Lunar Planet. Sci.* **33,** 1620.

Stolper E. (1982) Crystallization sequences of Ca-Al–rich inclusions from Allende: An experimental study. *Geochim. Cosmochim. Acta* **46,** 2159–2180.

Stolper E. and Paque J. M. (1986) Crystallization sequences of Ca-Al–rich inclusions from Allende: The effects of cooling rate and maximum temperature. *Geochim. Cosmochim. Acta* **50,** 1785–1806.

Wark D. A. (1987) Plagioclase-rich inclusions in carbonaceous chondrite meteorites: Liquid condensates? *Geochim. Cosmochim. Acta* **51,** 221–242.

Wark D. A. and Lovering J. F. (1977) Marker events in the early evolution of the solar system: Evidence from rims on Ca-Al–rich inclusions in carbonaceous chondrites. *Proc. Lunar Planet. Sci. Conf.* **8,** 95–112.

Wark D. A. and Lovering J. F. (1982) The nature and origin of type B1 and B2 Ca-Al–rich inclusions in the Allende meteorite. *Geochim. Cosmochim. Acta* **46,** 2581–2594.

Weber D. and Bischoff A. (1997) Refractory inclusions in the CR chondrite Acfer 059–El Djouf 001: Petrology, chemical composition, and relationship to inclusion populations in other Types of carbonaceous chondrites. *Chem. Erde.* **57,** 1–24.

Weisberg M. K., Prinz M., Zolensky M. E., Clayton R. N., Mayeda T. K., and Ebihara M. (1996) Ningqiang and its relationship to oxidized CV3 chondrites (abstract). *Meteorit. Planet. Sci.* **31,** A150–A151.

Yoneda S. and Grossman L. (1995) Condensation of CaO-MgO-Al_2O_3-SiO_2 liquids from cosmic gases. *Geochim. Cosmochim. Acta* **59,** 3413–3444.